Flux motion in thin superconductors with inhomogeneous pinning

Thomas Schuster, Holger Kuhn, and Ernst Helmut Brandt
Max-Planck-Institut für Metallforschung, Institut für Physik, D-70506 Stuttgart, Germany

Mikhail Indenbom
Institute of Solid State Physics, Russian Academy of Science, 142432 Chernogolovka, Russia

Michael R. Koblischka
Vrije Universiteit Amsterdam, Faculteit Natuurkunde en Sterrenkunde, De Boelelaan 1081, 1081 HV Amsterdam, The Netherlands

Marcin Konczykowski
Laboratoire des Solides Irradiés, Ecole Polytechnique, 91128 Palaiseau, France
(Received 27 June 1994)

The penetration and exit of magnetic flux in thin superconductors in a perpendicular applied field is investigated in detail. Flux-density pictures and profiles are obtained by magneto-optics; magnetization curves are measured by torque magnetometry; theoretical space- and time-dependent flux-density and current-density profiles are calculated from Maxwell's equations in a planar approximation assuming a highly nonlinear current-voltage law $E \sim (J/J_c)^n$ ($n \gg 1$, E = electric field, J = sheet current) with a critical sheet current $J_c(B, \mathbf{r})$ in general depending on the position and on the perpendicular flux density B. Our experiments and calculations show that for *inhomogeneous* pinning the additional nontrivial condition $J_c = \infty$ for $B = 0$ is appropriate. Our specimens are high-T_c superconductors in the form of platelets, strips, or rings. In two platelets, an inhomogeneous J_c was produced by heavy-ion irradiation of the edge zone or by thinning down the central part by sputtering. In all cases good qualitative agreement is found between the experimental and theoretical results. In particular, our time-dependent theory reproduces the recently derived static Bean-model profiles in perpendicular geometry, which we also confirm experimentally; field and current profiles in the ring are as predicted for a current-carrying strip in perpendicular field; in the platelet with enhanced edge pinning, when flux starts to leak into the central weak pinning zone the flux lines are driven immediately to the sample center and pile up there; for weaker inhomogeneity of $J_c(\mathbf{r})$, when the flux front arrives from the edges at the central weak-pinning zone the flux lines jump to an intermediate position from where they fill the central zone gradually. Our experiments also confirm the predicted "uphill motion" of flux lines *against* the flux-density gradient and the occurrence of overcritical current densities in the flux-free regions.

I. INTRODUCTION

An important property of type-II superconductors is their critical current density j_c at which the Abrikosov vortices depin and start to move under the influence of the Lorentz force. This vortex drift induces an electric field E which causes a voltage drop along the specimen. Consequently, at current densities $j > j_c$ energy is dissipated and the resistivity $\rho = E/j$ becomes finite. In high-T_c superconductors (HTSC's) thermally activated depinning of flux lines causes energy losses even at $j < j_c$. HTSC's are, therefore, better characterized by their nonlinear current-voltage law $E = E(j)$, which defines j_c as the current density at which $E(j)$ deviates noticeably from zero and starts to rise steeply, e.g., exponentially or according to a power law $E = (j/j_c)^n E_0$ with $n \gg 1$. The finite E at $j < j_c$ leads to the decay of persistent currents and to a decrease of the magnetic moment with approximately logarithmic time law (flux creep). While critical current densities may be determined from the width of the irreversible magnetization curve, time-resolved dc and ac methods in principle allow a contact-free measurement of the current-voltage characteristics. In all these experiments, maximum magnetic response is achieved when the specimen is a flat platelet or a thin film and the magnetic field H_a is applied perpendicular to the specimen.

A useful and instructive supplement to measurements of the integral magnetic moment is the observation of flux-density profiles at the specimen surface by magnetooptical techniques[1–8] or by Hall probes.[9–11] These space-resolved methods in principle allow the determination of $j_c(B, \mathbf{r})$ and $E(j, \mathbf{r})$ even in inhomogeneous superconductors. Moreover, the magneto-optical technique provides a powerful tool to verify theoretical models, e.g., of flux penetration and exit and of flux creep. The present paper presents a step towards this general goal.

If flux creep can be neglected, e.g., at low temperatures T or short times t, the current and flux densities inside a type-II superconductor often are successfully de-

scribed by the Bean critical state model,[12] which assumes a B-independent j_c. For long specimens in a longitudinal field, the Bean model predicts that $|j| = j_c$ in the region penetrated by flux, and $j = 0$ in the nonpenetrated regions; consequently, in regions with $B \neq 0$ one has $|\mathrm{curl}\mathbf{B}| \approx \mu_0 j_c = \mathrm{const}$, or $|dB/dx| = \mathrm{const}$ in planar geometry. Flux creep in this longitudinal Bean critical state recently has been described in a very general theory.[13] Numerous extensions to models with B-dependent j_c were developed, which shall not be discussed here. The modification of the Bean model at low inductions $B < B_{c1}$ (B_{c1} = lower critical field) has been modeled recently in a comprehensive work.[14] Throughout the present paper we shall assume $B_{c1} = 0$, leading to the simple relationship $B = \mu_0 H$ between the local induction B and the local magnetic field H in nonmagnetic materials.

The extension of the Bean critical state model to the more realistic perpendicular geometry was considered by various authors who computed the field profiles $B(\mathbf{r})$ for given current distributions with constant modulus $|j(\mathbf{r})| = j_c$ in disks.[15–17] A numerical inversion of this method has been performed successfully in Ref. 18 to obtain the space-resolved current density $j(r)$ from the perpendicular field component $B(r)$, which was measured magneto-optically at the surface of a superconducting disk. An elegant method to measure the current distribution in thin film strips uses a compensation method which directly yields the parallel field component above the superconductor surface.[19] Some analytical calculations for specimens with finite thickness and constant $|j| = j_c$ are given in Refs. 20 and 21.

Very recently, exact analytical solutions have been obtained within the planar approximation for the current and field profiles in thin circular disks[22,23] and long strips[24–26] with $|j| \leq j_c = \mathrm{const}$ in a perpendicular magnetic field. The low-frequency nonlinear magnetic response is obtained from these static solutions.[22–28] At higher frequencies, or if flux creep is considered, a time-dependent theory of superconducting disks or strips in a perpendicular field is required. If we assume j not to vary over the specimen thickness, this dynamic theory can be formulated in terms of a one-dimensional integral equation[29–31] (Sec. II), which is easily solved on a personal computer. If the resistivity is *linear*, complex and frequency dependent (e.g., due to thermally assisted flux flow or in the vortex-glass state at small amplitudes), one may calculate the linear ac susceptibility in this way and use this general result to extract the complex resistivity and its scaling behavior from contact-free magnetic ac measurements.[32] With appropriate *nonlinear* resistivity inserted, this equation allows one to compute the flux penetration into strips, disks, or rings, and the penetration and exit of flux when the applied field $H_a(t)$ is cycled, and flux creep when H_a is kept constant.[33] Very recently, an exact analytical solution of this nonlinear and nonlocal diffusion equation for flux creep was obtained,[34] which extends the results of Ref. 13 to perpendicular geometry.

The present paper compares the flux profiles measured by magneto-optics (Sec. III) on strips, rectangular platelets, rings, and platelets with inhomogeneous J_c (generated by irradiation of the edge zone and by sputtering) with the calculated profiles (Sec. IV). Examples for B-dependent j_c and for flux creep are also given. Conclusions are drawn in Sec. V.

II. THEORY

A. Nonlocal current-field relationship

Within continuum theory, the time- and space-dependent distribution of magnetic flux and current density in a type-II superconductor with bulk pinning and with $B \approx \mu_0 H$ (i.e., if one may put $H_{c1} = 0$) in an applied field $H_a(t)$ is completely determined by the resistivity $\rho(j) = E(j)/j$ of the specimen and by its geometry. We disregard here possible effects of a surface barrier; in our opinion, in type-II superconductors (and type-I superconductors[35]) the observation of an asymmetric irreversible magnetization curve is due to a macroscopic "edge-shape barrier"[36–39] rather than to a microscopic Bean-Livingston barrier.[40] This geometric barrier occurs in flat specimens with constant thickness but not in ideal ellipsoids.

In this section we consider strips (along z) with width $2a$ ($-a \leq y \leq a$) and disks with radius a ($r \leq a$), both with thickness $d \ll a$ ($-d/2 \leq x \leq d/2$). Integrating the current density over the thickness we get the sheet current $\mathbf{J}(y,z) = \int_{-d/2}^{d/2} \mathbf{j}(x,y,z)\,dx$. Ampère's law then yields for the magnetic field $\mathbf{H} = (H_x, H_y)$ around the strip in the planar approximation (neglecting terms of order d/a) (Ref. 24)

$$\mathbf{H}(x,y) = \mathbf{H}_a + \frac{1}{2\pi}\int_{-a}^{a} \frac{(y-u,\,-x)\,J(u)}{(y-u)^2 + x^2}\,du\,. \qquad (1)$$

Noting that for $|x| \ll a$ the term $x/[(y-u)^2 + x^2]$ in the integrand may be replaced by $\pi\,\delta(y-u)\,\mathrm{sgn}(x)$ [$\delta(x)$ = Dirac's delta function, $\mathrm{sgn}(x)$ = sign of x] we obtain for the parallel field component near the surface of the strip $H_y(x,y) = -\mathrm{sgn}(x)J(y)/2$ plus terms of order d/a. This result expresses the well-known fact that the jump of H_y equals the sheet current. For the perpendicular field $H_x(x,y)$ we get from (1), using the symmetry of the shielding current $J(-y) = -J(y)$ in the strip,

$$H_x(x,y) = H_a + \frac{1}{2\pi}\int_0^a J(u) \times\left[\frac{y-u}{(y-u)^2 + x^2} - \frac{y+u}{(y+u)^2 + x^2}\right]du\,. \qquad (2)$$

Up to terms of order d/a this yields at the strip surfaces the perpendicular field component $H_x(y) = H(y)$,

$$H(y) = H_a + \frac{1}{2\pi}\int_0^a \frac{2u\,J(u)}{y^2 - u^2}\,du\,. \qquad (3)$$

Similarly, one finds at the surfaces of a disk in which a sheet current $J(r)$ circulates,

$$H(y) = H_a + \frac{1}{2\pi}\int_0^a P(r,u)\,J(u)du, \tag{4}$$

where the integral kernel $P(r,u) = -p\,(r/u)/u$ with

$$p\,(v) = \int_0^\pi \frac{v^{-1}\cos\phi - \cos^2\phi}{(1+v^2-2v\cos\phi)^{3/2}}\,d\phi \tag{5}$$

may be expressed in terms of complete elliptic integrals.[31] One has $p\,(v) = \pi + (3\pi/4)v^2$ for $v \ll 1$, $p\,(v) = -\pi/2v^3 - 9\pi/16v^5$ for $v \gg 1$, and $p\,(v) = -1/(v-1) + \ln(4/|v-1|)$ for $v \approx 1$. The angular integral (5) is easily evaluated using constant weights, or better, by substituting $\phi = \phi(x) = x - (1/3)\sin x\,(4 - \cos x)$ with $\phi'(x) = (2/3)(1-\cos x)^2$ and using equidistant integration points $x = x_i = (i - \frac{1}{2})\pi/N$, $i = 1, ..., N$, with weights $\phi'(x_i)\pi/N$. This substitution stretches the integrand near its maximum (occurring at $\phi = 0$) and yields accurate results even when v is close to unity.

B. Statics

The essential results for the Bean critical state in a strip in perpendicular geometry[24–26] in the planar approximation are as follows. Defining a critical sheet current $J_c = j_c d$ and a critical field $H_c = J_c/\pi$, one may write the sheet current $J(y)$ and the perpendicular magnetic field $H(y)$ in a field $H_a(t)$ which is slowly increased from zero as

$$J(y) = \begin{cases} \dfrac{2J_c}{\pi}\arctan\dfrac{cy}{(b^2-y^2)^{1/2}}, & |y| < b, \\ J_c\,y/|y|, & b < |y| < a, \end{cases} \tag{6}$$

$$H(y) = \begin{cases} 0, & |y| < b, \\ H_c\,\mathrm{arctanh}\dfrac{(y^2-b^2)^{1/2}}{c\,|y|}, & b < |y| < a, \\ H_c\,\mathrm{arctanh}\dfrac{c\,|y|}{(y^2-b^2)^{1/2}}, & |y| > a, \end{cases} \tag{7}$$

where

$$b = a/\cosh(H_a/H_c), \tag{8}$$

$$c = (a^2-b^2)^{1/2}/a = \tanh(H_a/H_c). \tag{9}$$

Here b denotes the position of the flux front and $a - b$ is the penetration depth of the magnetic flux. Integrating (6) and (7) one obtains the magnetic moment $M = 2\int_0^a y\,J(y)\,dy$ and the penetrated flux $\Phi = 2\int_0^a H(y)\,dy$ per unit length of the strip (throughout this paper M denotes the *negative* magnetic moment),

$$M = J_c a^2 c = J_c a^2 \tanh\,(H_a/H_c)\,, \tag{10}$$

$$\Phi = 2\mu_0 H_c a \ln(a/b) = 2\mu_0 H_c a \ln\cosh(H_a/H_c)\,. \tag{11}$$

The sheet current $J(r)$ in a disk of radius a is also given by Eq. (6) but with y replaced by r and with $H_c = J_c/\pi$ replaced by $H_c = J_c/2$ in Eqs. (8) and (9). The perpendicular field $H(r)$ at the disk surface and the penetrated flux Φ then follow by inserting this $J(r)$ into Eq. (4); analytical solutions for $H(r)$ are not available for the disk. The (negative) magnetic moment $M = \pi\int_0^a r^2\,J(r)\,dr$ of the disk is[22]

$$M = (8/3)H_a a^3 S(H_a/H_c)\,,$$
$$S(x) = \frac{1}{2x}\left[\arccos\frac{1}{\cosh x} + \frac{\sinh|x|}{\cosh^2 x}\right], \tag{12}$$

with $H_c = J_c/2$. In particular one has for $H_a \ll H_c$ ($H_a \gg H_c$) $M = \pi H_a a^2$ ($M = J_c a^2$) for the strip per unit length, and $M = 8H_a a^3/3$ ($M = \pi J_c a^3/3$) for the disk since $S(0) = 1$ and $S(x \gg 1) = \pi/(4x)$.

From these virgin solutions one may obtain the general solutions for arbitrary magnetic history $H_a(t)$. For example, if $H_a(t)$ is cycled between the values $+H_0$ and $-H_0$, one obtains in the half period with decreasing H_a

$$\begin{aligned} J_\downarrow(y,H_a,J_c) &= J(y,H_0,J_c) - J(y,H_0-H_a,2J_c)\,, \\ H_\downarrow(y,H_a,J_c) &= H(y,H_0,J_c) - H(y,H_0-H_a,2J_c)\,, \\ M_\downarrow(H_a,J_c) &= M(H_0,J_c) - M(H_0-H_a,2J_c)\,, \\ \Phi_\downarrow(H_a,J_c) &= \Phi(H_0,J_c) - \Phi(H_0-H_a,2J_c)\,. \end{aligned} \tag{13}$$

At $H_a = -H_0$ the original virgin state is reached again but with J, H, M, and Φ having changed sign. In the half period with increasing H_a one has $J_\uparrow(y,H_a,J_c) = -J_\downarrow(y,-H_a,J_c)$, $H_\uparrow(y,H_a,J_c) = -H_\downarrow(y,-H_a,J_c)$, $M_\uparrow(H_a,J_c) = -M_\downarrow(-H_a,J_c)$, and $\Phi_\uparrow(H_a,J_c) = -\Phi_\downarrow(-H_a,J_c)$. Note that the relationships (13) apply also to longitudinal geometry, where they are trivial. They are, however, restricted to models where J_c does not depend on field and position. The invalidity of (13) for inhomogeneous pinning is connected with the formal appearance of "overcritical" currents discussed below in Sec. VI D.

The planar *magnetostatics*, Eqs. (1)–(13), applies even when the current density $\mathbf{j}(\mathbf{r})$ varies over the specimen thickness, e.g., when the screening currents are not Meissner currents but currents in a usual (longitudinal) Bean critical state generated across the thickness by the sheet current. However, in the following *dynamic* planar problem one has to assume constant j (and E) over the thickness in regions where the electric field $E \neq 0$. This condition holds for thicknesses d smaller than the magnetic penetration depth λ, but according to our results below, the dynamic planar approximation works well even with thicker specimens and yields the correct static profiles.

C. Dynamics

The Bean model of Sec. II B applies to steplike current-voltage characteristics, $E(j < j_c) = 0$ and $E(j > j_c) = \infty$. For smooth $E(j)$, occurring at finite T in HTSC's, the results J, H, M, and Φ depend on the time t; i.e., the ramp rate $\dot{H}_a(t) = dH_a/dt$ enters or, if $\dot{H}_a = 0$, flux creep occurs. The equation of motion for the sheet current $J(y,t)$ or $J(r,t)$ is then derived from Faraday's induction law as follows.

When the magnetic flux $\phi(y) = \mu_0 L \int_0^y H(u)du$ or $\phi(r) = 2\pi\mu_0 \int_0^r H(u)udu$ threading part of the strip (of length L) or disk varies with time, it induces an electric field $E(y,t) = \dot{\phi}(y,t)/L$ or $E(r,t) = \dot{\phi}(r,t)/2\pi r$ along the boundary of this area. Inserting here Eq. (3) or (4) and $E = \rho(J)J/d$ (for the dynamics, we assume that $j = J/d = \text{const}$ over the sample thickness in regions where $E \neq 0$) one gets the integro-differential equations for the sheet current $J(y,t)$ (strip) and $J(r,t)$ (disk),[29–31]

$$J(y,t) = \tau\left[2\pi y\dot{H}_a(t) + \int_0^1 \dot{J}(u,t)\,K(y,u)\,du\right], \quad (14)$$

$$J(r,t) = \tau\left[\pi r\dot{H}_a(t) + \int_0^1 \dot{J}(u,t)\,Q(r,u)\,du\right]. \quad (15)$$

Here $\tau = \tau(J) = ad\mu_0/2\pi\rho(J)$ is a relaxation time, which in general may depend on B and J (via ρ) and on the position $\mathbf{r}$ (via ρ, B, or J, or if the thickness d depends on $\mathbf{r}$). In Eqs. (14) and (15) the half width or radius a is chosen as the unit length and the integral kernels are

$$K(y,u) = \ln\left|\frac{y-u}{y+u}\right|, \quad Q(r,u) = -q\left(\frac{r}{u}\right),$$

$$q(v) = \int_0^\pi \frac{\cos\phi}{(1+v^2-2v\cos\phi)^{1/2}}\,d\phi; \quad (16)$$

cf. Eq. (5). One has $q(1/v) = vq(v)$, $q(v) \approx (\pi/2)v + (3\pi/16)v^3$ for $v \ll 1$, and $q(v) \approx 0.079\,44 - \ln|1-v|$ for $v \approx 1$.

Equation (14) or (15) may be integrated over time t on a personal computer by a method described in Ref. 30. From the resulting sheet current the magnetic field $H(y,t)$ or $H(r,t)$ is obtained by (3) or (4). For a sufficiently sharply bent current-voltage law $E(j)$, this time integration reproduces the analytical solutions of the perpendicular Bean model of Sec. II B. The time step during this integration should be chosen to be proportional to $\tau(J) \sim 1/\rho(J) = j/E(j)$; in this way high numerical stability and speed is achieved, and in the case of flux creep[34] the numerical time scale effectively becomes logarithmic such that creep over a large time interval of many orders of magnitude can be simulated.

D. Examples

Throughout this paper we shall use the model current-voltage law $E(j) \sim j^n$ ($n \gg 1$) which corresponds to a logarithmic activation energy $U(j) \sim \ln(j/j_1)$, or to $U(j) \sim j^{-\alpha}$ with $\alpha \ll 1$. For our computation we chose units E_0 for the electric field, j_0 for the current density, and $J_0 = j_0 d$ (d = specimen thickness) for the sheet current and magnetic field. We write $E(j) = (j/j_c)^n E_c$ with $n = 19$; here j_c has the meaning of a critical current density which in general may depend on B and $\mathbf{r}$, implicitly via $B = B(\mathbf{r})$ or explicitly in inhomogeneous materials. We keep $E_c = E_0 = \text{const}$ in the following simulations; another choice would be to keep $j_c = j_0 = \text{const}$ and choose $E_c = E_c(B,\mathbf{r})$; for our power law $E(j)$ both choices are physically identical. The exponent $n = 19$ is chosen to allow studies of both the Bean critical state ($n \to \infty$) and creep effects; a choice $n < 10$ would smear the flux front markably due to rapid flux creep, while $n > 100$ would require long simulation times to see creep effects. The choice of a power law, exponential, or other highly nonlinear current-voltage characteristics is not crucial in our simulations.[34] Noting that the critical sheet current J_c may depend on $\mathbf{r}$ also via a varying specimen thickness, $J_c(B,\mathbf{r}) = j_c(B,\mathbf{r})d(\mathbf{r})$, we write our planar model

$$E(J) = [J/J_c(B,\mathbf{r})]^{19}E_0, \quad B = B_x = \mu_0 H_x. \quad (17)$$

The induced sheet current $J(y)$ and penetrating magnetic field $H(y)$ obtained by time integration of Eq. (14) for a strip in increasing applied field are depicted in Figs. 1 and 2. Very similar results are obtained for circular disks. In Fig. 1 constant $j_c = j_0$ was assumed, resulting in a saturation of $J(y)$ to a value $\approx 1.05J_c$ ($J_c = j_c d$) in

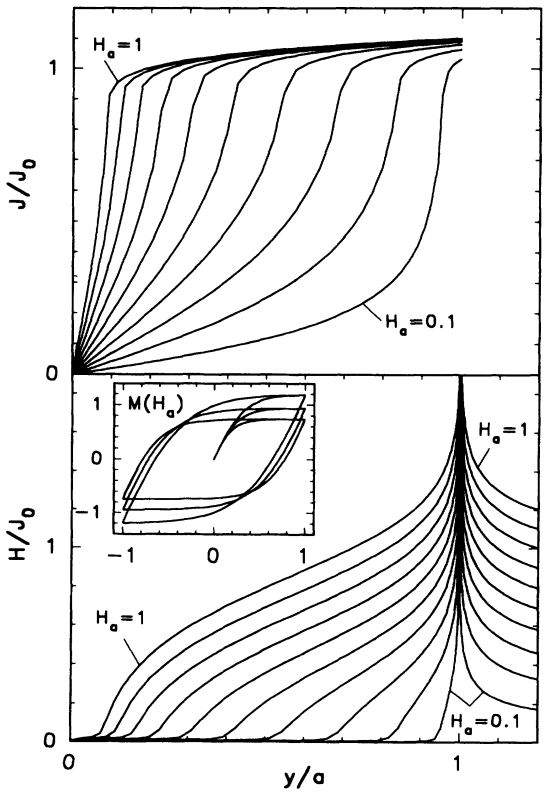

FIG. 1. Flux penetration into a strip with half width a and with current-voltage law $E(j) = (j/j_c)^{19}E_0$ with $j_c = j_0 = \text{const}$. Depicted are the sheet current $J(y)$ and perpendicular field $H(y)$ (both in units $J_0 = j_0 d$) in increasing applied field $H_a = 0.1, 0.2, 0.3, 0.4, 0.5, 0.7, 0.8, 0.9, 1$ in units J_0. The ramp rate was $dH_a/dt = 1$ in units $E_0/a\mu_0$. The nonsteplike $E(j)$ smears the vertical slopes of $J(y)$ and $H(y)$ at the flux front as compared to the Bean model and yields a slightly varying $J(y)$ in the penetrated region. The inset shows the magnetization curves of this model for three sweep rates $dH_a/dt = 1$, 10^{-2}, and 10^{-4}.

the penetrated region. This factor of 1.05, rather than a factor of 1, depends on the ramp rate $\dot{H}_a = dH_a/dt$ or sweep rate $|\dot{H}_a|$; in Figs. 1 and 2 we chose $|\dot{H}_a| = 1$ in our units $E_0/a\mu_0$. For comparison, below in Figs. 9 and 10 we shall use a much slower sweep rate $|\dot{H}_a| = 0.01$, which yields a saturation current of $\approx 0.8J_c$. Note that any finite ramp rate allows for flux creep, which reduces $J(y)$ and causes a slightly positive slope of $J(y)$. The effect of flux creep is also seen in the magnetization curves $M(H_a)$ presented for the same models in the insets of Figs. 1 and 2 for H_a cycled with three different sweep rates $|\dot{H}_a| = 1$, 10^{-2}, and 10^{-4}. Note that the initial slope of the virgin curve is independent of the sweep rate; see text below Eq. (12).

The saturated current density in disks and rings can be estimated, and in double strips or rings even be calculated exactly, as follows.

After complete penetration of H, the sheet current J saturates and becomes time independent when H_a is increased further with rate $\dot{H}_a$. In this stationary situation the electric field in the specimen follows from the induction law $\nabla \times \mathbf{E} = -\dot{\mathbf{B}}$. Using the inversion symmetry of J one gets for the strip $E(y) = y\mu_0\dot{H}_a$ and for the disk $E(r) = r\mu_0\dot{H}_a/2$; cf. Eqs. (14) and (15). From this E, $J = jd$ is obtained by inverting the $E(j)$ law. Our model (17) means $j(\mathbf{r}) = j_c(B,\mathbf{r})[E(\mathbf{r})/E_0]^{1/19}$. This yields for a strip with $j_c = j_0 = \text{const}$ the saturated sheet current $J(y) = J_c(y\mu_0\dot{H}_a/E_0)^{1/19}$. With $\dot{H}_a$ in reduced units $E_0/\mu_0 a$ one has $J(y)/J_c = (y\dot{H}_a/a)^{1/19}$, which is nearly constant except close to the strip center $y = 0$. This result is a good approximation in the penetrated region even *before* penetration is complete. Note that for the strip complete penetration of H occurs at a rather large applied field $H_a \approx (j_c d/\pi)\ln(4a/d)$ obtained from (7). If the center of the thin specimen is cut out, e.g., in a double strip or ring, then complete penetration occurs at a smaller field H_a, which remains finite even in the limit of zero specimen thickness d.[25] In this geometry the saturated electric field $E \sim y$ or $E \sim r$ is *exact*; the exact current density j is then obtained by inserting this $E(\mathbf{r})$ into the material law $j(E)$, and the exact magnetic field $H(\mathbf{r})$ is obtained by inserting $J = jd$ into (3) or (4).

The qualitative agreement of the profiles $J(y)$ and $H(y)$ in Fig. 1 with the predictions (6) and (7) of the Bean model is obvious. Due to our smooth $E(j)$, the ideally vertical slopes of $J(y)$ and $H(y)$ at the flux front are smeared. If we use a steeper $E(j) = (j/j_c)^{99}E_0$, our "dynamic" results coincide with the "static" analytical results (6) and (7) within line thickness.

Figure 2 shows a similar penetration of flux into a strip, but now j_c is allowed to depend on the local flux density B. In Fig. 2 the model $j_c = j_0/(0.8 + |H|)$ (with $H = B/\mu_0$ in our units $J_0 = j_0 d$) is chosen, but other models like $j_c = j_0\exp(-|H|)$ yield very similar results. Notice that realistic $j_c(B)$ with monotonically decreasing j_c do *not* remove the logarithmic infinity of the perpendicular field component $H(y)$ at the specimen edge and its vertical slope at the flux front. Remarkably, the B dependence of j_c even leads to a sharp cusp in the current density $J(y)$ at the flux front, which is clearly seen in Fig. 2. The magnetization curves depicted in the inset of Fig. 2 for three sweep rates clearly show the decrease of j_c at larger fields $|H_a|$; cf. also Fig. 11.

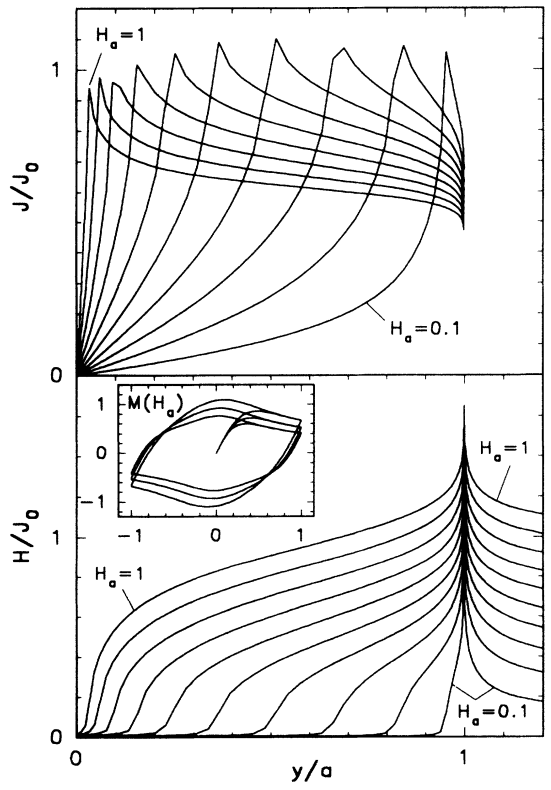

FIG. 2. As Fig. 1 but for field-dependent critical current density $j_c(H) = j_0/(0.8 + |H|)$ which enters the current-voltage law $E(j) = [j/j_c(H)]^{19}E_0$.

III. EXPERIMENTS

A. Faraday effect

To visualize the magnetic field distribution of a superconductor we use the magneto-optical Faraday effect. The flux penetration is imaged by detecting the rotation of the polarization plane when linearly polarized light passes a magneto-optically active layer exposed to the magnetic field of the underlying superconductor. From flux-free regions the light is reflected without rotation of the polarization plane; this light thus cannot pass the analyzer which is set in a crossed position with respect to the polarizer. In this way the Shubnikov phase (with a flux-line lattice) will be imaged as bright areas, whereas the flux-free Meissner phase remains dark.

Since the HTSC's themselves do not show a significant Faraday effect, the sample surfaces have to be covered by a magneto-optically active material. For the experiments presented in this paper, EuSe thin films and ferrimagnetic iron garnet films with an in-plane anisotropy were used as magneto-optical indicators. The EuSe thin

films were deposited by electron-beam evaporation directly onto the sample surface, which was coated before with an aluminum layer (thickness about 200 nm), in order to enhance its reflectivity.[6] This technique allows flux distributions to be observed directly with a spatial resolution of about 1 μm in a temperature range of 5 K $\leq T \leq$ 20 K. The lower-temperature boundary is given by the cryostat used; the upper limit is imposed by the temperature dependence of the Verdet constant of the europium chalcogenides, which leads to very low rotation angles at higher temperatures.[2] However, flux distributions at temperatures $T >$ 20 K can be visualized indirectly by a special procedure during which the flux distribution obtained at a given temperature is observed after cooling the sample down to 5 K. This technique gives the correct flux patterns because j_c becomes larger when the temperature is decreased; therefore, the sample at lower temperatures enters an undercritical state; i.e., the flux distribution is not changed.[41]

The iron garnet film was deposited by liquid phase epitaxy onto a gallium-gadolinium substrate with a thickness of about 3.5 μm (commercial firm Gamma Scientific Production, Russia).[8] This kind of indicator allows the flux penetration into HTSC samples to be observed directly in the whole temperature regime of superconductivity with a higher magnetic sensitivity than with the EuSe thin films. However, its spatial resolution is limited by the thickness of the indicator to about 4 μm. The superconductor was glued onto this substrate by the glue "Leit-C."

The external magnetic field is generated by a copper solenoid coil, which is cooled with liquid nitrogen and produces a maximum field of 0.6 T. The observations were performed in the optical cryostat described in Refs. 6 and 42. All images can be observed directly via the microscope or be transferred to an image processing system for analyzing.[43] The image processing system allows one to determine the grey level pixel by pixel along a user-defined line.

To calibrate the measured intensity I in terms of the local flux density B_x, two fixed points are determined: In the Meissner phase at the center of the sample we have $B_x = 0$. Far away from the sample edge on the substrate, the measured intensity corresponds to the external field $\mu_0 H_a$. Using these fixed points, the measured intensity can be directly related to B_x.[44] In the field range interesting for our experiments, the field-intensity characteristics are approximately linear except near $B_x = 0$ (in crossed polarizer-analyzer setting).

B. Magnetization measurements

Magnetization curves were obtained from torque hysteresis loops which were measured by a capacitance technique.[45] In our setup the direction of the external magnetic field is fixed whereas the sample can be rotated by an angle θ defined as the angle between the c axis of the sample and the external magnetic field H_a. Torque magnetometry[46,47] measures the magnetic torque

$$\tau = \mathbf{M} \times \mathbf{H}_a \quad . \tag{18}$$

The extreme orientations at $\theta = 0°$ and $\theta = 90°$ are not accessible to the torque measurements because in both cases M is aligned parallel to H_a. For this reason, the measurements were performed at an angle $\theta = 8°$, assuming that this small deviation from the direction $H_a \parallel c$ (and, therefore, H_a parallel to the columnar defects) does not influence our results. From the torque data, the corresponding magnetization is calculated via Eq. (18).

The advantage of the torque measurements in comparison to, e.g., superconducting quantum interference device (SQUID) measurements is the speed of measurement, limited only by the sweep rate of the magnet. This allows one to investigate also the sweep-rate dependence of the hysteresis loops, and to calculate from this the dynamic relaxation rate Q.[48]

C. Sample preparation and irradiation

The c-axis-oriented $YBa_2Cu_3O_{7-\delta}$ (YBCO) thin films were produced at the Max-Planck-Institut für Festkörperforschung (Stuttgart, Germany) by a laser-ablation technique with a film thickness of 300 nm.[49] All thin films were patterned chemically to be used for four-terminal measurements.

For investigations of inhomogeneous pinning we used $Bi_2Sr_2CaCu_2O_{8+\delta}$ (Bi2212) single crystals which were prepared with thicknesses of about 30 μm as described in Ref. 50. To obtain regions with large differences in their pinning forces the samples were irradiated through a mask by 860 MeV Xe ions at GANIL (Caen, France). This high-energy heavy-ion irradiation produces columnar defects which prove to be very effective pinning sites in HTSC's (Ref. 51) and increase the critical current density by factors of at least 20–50 depending on temperature and fluence; at T = 50 K the unirradiated sample possibly was even above the depinning line; see the measurements by D'Anna *et al.*[52] who found with the same specimen a depinning field below 1 mT at T = 40 K. During the irradiation, the center of the sample was covered by an absorber to expose only the outer regions of the sample to the ion beam, Fig. 19(a). Later the absorber was removed by an organic solvent. In other specimens, to obtain small differences in the pinning strength, the central region of the crystal was thinned down to about half the original thickness.

IV. RESULTS AND DISCUSSION

A. Strip

In this section we compare theoretical calculations of the magnetic field distribution with experimentally measured flux-density profiles of an YBCO strip with homogeneous pinning. This simple example allows one to check the field profiles obtained from our magneto-optic intensity profiles. Note also that only for this geometry an analytical solution for the field distribution is available, Eq. (7). For a strip with inhomogeneous pinning an analytical solution was given very recently.[38]

In Fig. 3 the flux distribution of an YBCO strip (width

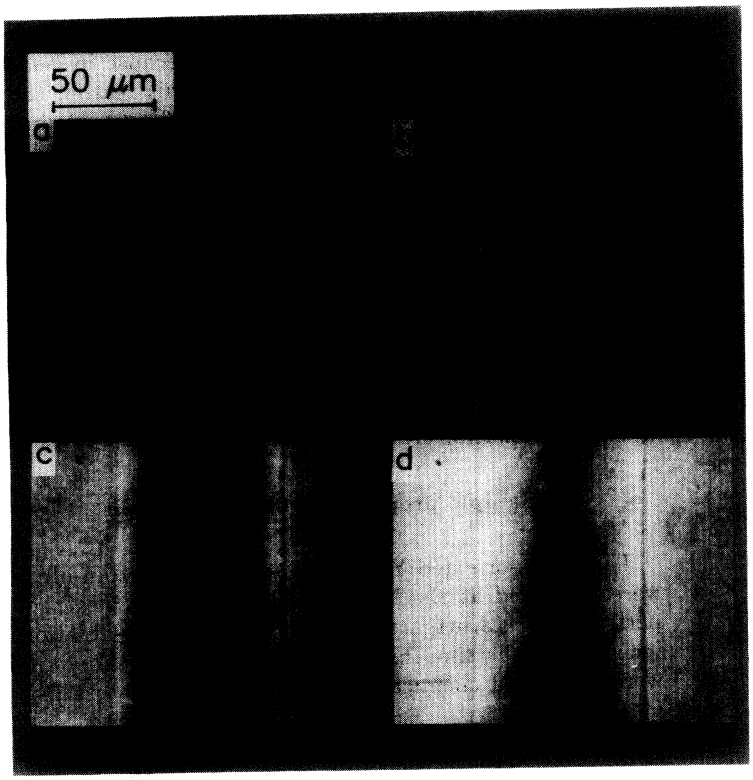

FIG. 3. Flux distributions of 82 μm wide and 300 nm thick YBCO strip obtained by means of EuSe as magneto-optical indicator. The external magnetic field $\mu_0 H_a$ is oriented perpendicular to the sample surface and hence parallel to the c axis. The bright areas of the sample show the Shubnikov phase; the dark regions correspond to the flux-free Meissner phase. (a) $\mu_0 H_a$ = 21 mT. The white arrows indicate the place where the profiles in Fig. 4 were measured. (b) $\mu_0 H_a$ = 53 mT, (c) $\mu_0 H_a$ = 107 mT, (d) $\mu_0 H_a$ = 160 mT.

$2a = 84$ μm, thickness $d = 300$ nm) is shown at $T = 5$ K in external magnetic fields of $\mu_0 H_a = 21$ mT (a), 53 mT (b), 107 mT (c), and 160 mT (d). The external magnetic field is oriented perpendicular to the sample surface and hence parallel to the c axis. The bright areas of the sample correspond to the Shubnikov phase, where flux lines have penetrated, and the flux-free Meissner phase remains dark. Because of nonsuperconducting precipitates at the sample surface, which result from the sample production process, the flux distribution is slightly disturbed: Since the supercurrent cannot pass through these precipitates, it has to flow around forming parabolic structures in the flux distribution [see Figs. 3(d) and 8]. Very recently the conditions of visualization and a detailed description of such parabolic structures were published.[53] The dark lines at the sample edges are due to a damage of the sample surface during the patterning process. At these places, the light is diffusely scattered. The white arrows in Fig. 3(a) indicate the line where the flux-density profiles shown in Fig. 4 were measured.

The flux-density profiles in Figs. 4(a) and 4(b) correspond to the flux distribution shown in Figs. 3(a), 3(b), and 3(d). The dotted profiles are the experimentally determined flux distributions whereas the calculated ones are drawn as solid lines. The influence of the sample edges on the measured intensity profiles was corrected by omitting some wildly oscillating data points which correspond to the sharp dark line marking this edge. The theoretical curves plotted in Fig. 4(a) were calculated from Eq. (7) by inserting the sample width $2a$, the position of the flux front b, the external magnetic field H_a, and the sample thickness d. Furthermore, from these four quantities we can determine the critical current density $j_c = 3 \times 10^{11}$ A/m^2 via Eq. (8), which is independent of H_a in the field range investigated here. Note that all these quantities are available from our experiment and thus fitting procedures are not necessary.

The measured data in general agree well with the calculated ones; however, we find some characteristic deviations: Due to a weak inhomogeneity of the sample, the flux penetration from the two sample edges is slightly different in this experiment. Therefore, on the right side of the sample the calculated profiles show a deeper penetration depth than the measured ones. Furthermore, at the flux front the theoretical profiles have a vertical slope in contrast to the experiment, and the logarithmic infinity of B_x at the sample edges causes an extreme overshoot of the theoretical profiles. As to the last two points, a better agreement of the theoretical and experimental data can be achieved by taking into account the finite height x above the sample midplane $x = 0$ of the evaporated EuSe and aluminum layers at which the profiles were measured. The corrected (smeared) profiles were calculated from Eq. (2) by inserting the current distribution of Eq. (6). In Fig. 4(b) the calculated curves (solid lines) are plotted together with the measured profiles; the excellent agreement between theory and experiment is evident.

An even better agreement is achieved if we consider the nonlinearity of the relation between the light intensity and the flux density B. In particular, the expected

quadratic dependence at low $|B|$ straightens the square-root singularities of $B \sim (|y| - b)^{1/2}$ predicted at the flux front by Eq. (7). This straightening is clearly seen in Fig. 4. However, since the exact gauging of the light intensity is difficult (depending, e.g., on rotations of the images in the optical system or magnetic stray fields at the position of the charge-coupled device camera), we do not account for this nonlinearity in the present paper.

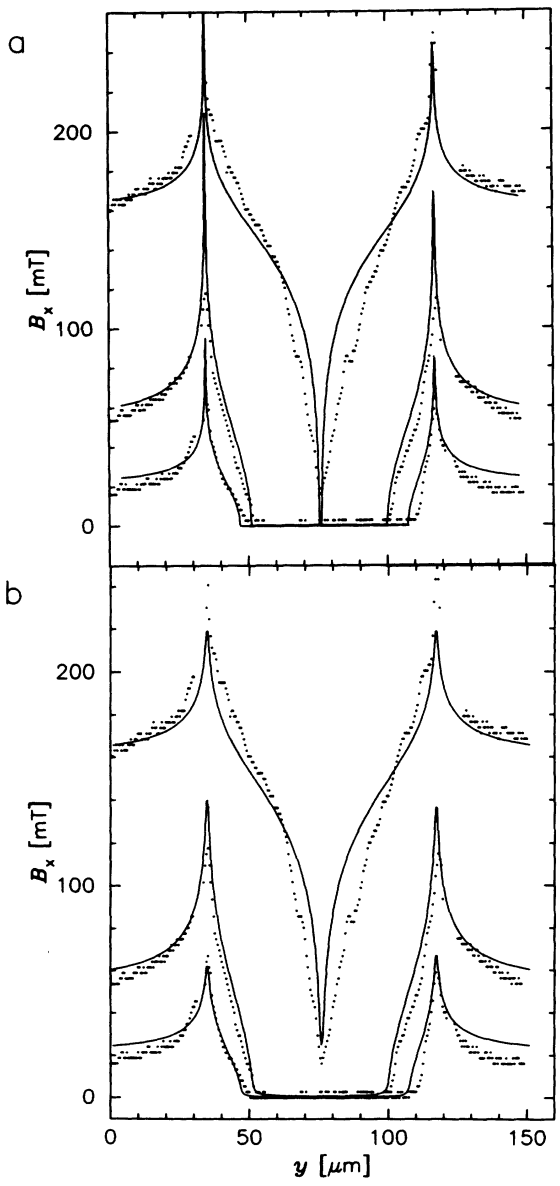

FIG. 4. Measured and calculated flux-density profiles of a thin strip corresponding to external magnetic fields of $\mu_0 H_a$ = 21 mT, $\mu_0 H_a$ = 53 mT, and $\mu_0 H_a$ = 160 mT [cf. Figs. 3(a), 3(b), and 3(d)]. (a) Measured flux distributions (dotted) of the thin strip presented in Fig. 3 and the corresponding profiles which were calculated from Eq. (7) (solid lines). (b) For a finite x Eq. (2) yields the solid curves. A better agreement than in (a) between the calculated and the measured (dotted) data is achieved. For details see text.

Figure 5 shows the flux distributions of the same YBCO strip after an external magnetic field of $\mu_0 H_0$ = 160 mT was applied and subsequently decreased to $\mu_0 H_a$ = 107 mT (a), 53 mT (b), and 0 mT [(c), remanent state of Fig. 3(d)]. In Fig. 5(d) a reversed field of $\mu_0 H_a = -53$ mT is applied to the remanent state. In decreasing external magnetic field the dark regions near the sample edges indicate a drastic decrease of B_x, Fig. 5(a) and 5(b). The drop of B_x is explained in Fig. 6: Figure 6(a) shows the spatial current distribution in a strip, which is obtained from Eqs. (6) and (13), while the external magnetic field is decreased from $H_a = H_0$ to $H_a = 0.9H_0$, $0.5H_0$, 0, $-0.5H_0$, and $-H_0$ (in order to achieve a clear arrangement H_0 is chosen so that the flux front is located at $y/a \approx 0.8$, which is in contrast to the experiment where full penetration is achieved). With a very small decrease of the external field the sheet current switches from $+J_c$ to $-J_c$; as a consequence the logarithmic infinity of H changes sign and is now opposed to the external field [see Fig. 6(b)], in contrast to the situation in increasing field.

The sharp decrease of the magnetic field at the sample edges while decreasing the external magnetic field is connected with the nucleation of vortices with opposite (negative) sign with respect to the pinned (positive) ones. These negative flux lines are generated at the sample edge by the stray field of the positive flux lines and, subsequently, when penetrating the sample, they annihilate the pinned vortices.[54–56] In the remanent state [Fig. 5(c)] the negative flux lines (white zone at the sample edge) and the pinned positive vortices are clearly visible. Note that in a crossed polarizer-analyzer setting the flux line polarities cannot be distinguished. While a reversed external magnetic field is increased, more negative flux lines penetrate into the superconductor [see Fig. 5(d)].

In Fig. 7 the measured flux-density profiles (dotted curves) are plotted together with the corresponding theoretically calculated curves (solid lines). The profiles were measured after increasing the external magnetic field to $\mu_0 H_0$ = 160 mT, and subsequently decreasing it to $\mu_0 H_a$ = 53 mT, 0 mT, −53 mT, and −160 mT. The negative B_x values were obtained by inverting the intensities of the respective data points. The data points at the dark lines which are due to the damaged surface at the edge zone are omitted here as in Fig. 4. The theoretical curves were calculated for finite x from Eqs. (2) and (13) and agree well with the experimentally measured profiles.

B. Rectangle

In order to get a better understanding of the very complex behavior of flux penetration which is presented in the following Secs. IV C and IV D, in this section, we will discuss the flux distribution of square-patterned YBCO thin films. In the experiments shown here and in the following sections, an iron garnet thin film was used as magneto-optical indicator. The sample is one of the pads for voltage measurements of the above mentioned four-terminal geometry. The external magnetic field was ap-

FIG. 5. Flux distributions on the same YBCO strip. In these experiments the external magnetic field is decreased from $\mu_0 H_a = 160$ mT to various external fields $\mu_0 H_a$. (a) $\mu_0 H_a = 107$ mT, (b) $\mu_0 H_a = 53$ mT, (c) $\mu_0 H_a = 0$ mT (remanent state), (d) $\mu_0 H_a = -53$ mT.

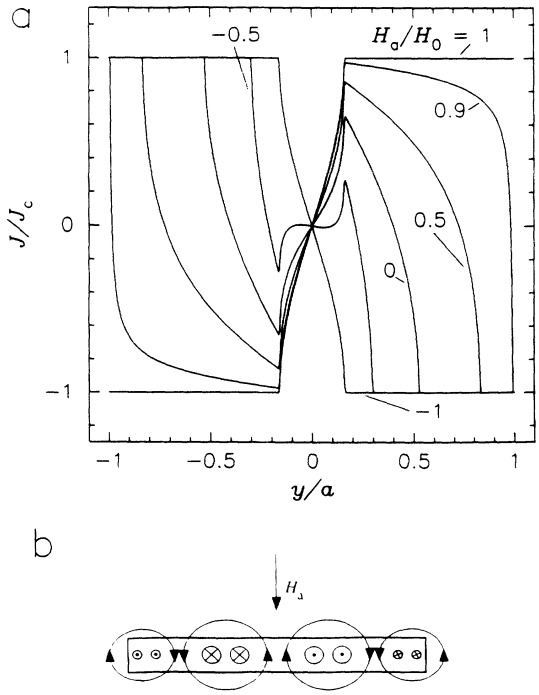

FIG. 6. (a) Calculated distribution of the sheet current $J(y)$ in decreasing external field H_a for $H_0 = 2.5H_c$ and $H_a/H_0 = 1$, 0.9, 0.5, 0, −0.5, and −1. The curves were obtained from Eqs. (6) and (13). (b) Sketch of the direction of current flow and the current-generated magnetic field during decrease of the external magnetic field. As long as the external field is not reversed, the current-generated field and the homogeneous external magnetic field are oriented antiparallel at the sample edge in contrast to the situation during virgin magnetization.

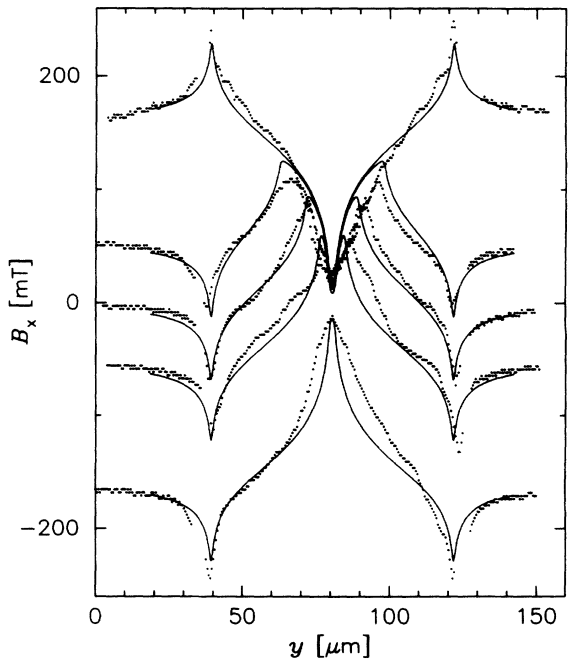

FIG. 7. Measured (dotted curves) and calculated flux-density profiles after application of an external magnetic field of $\mu_0 H_a = 160$ mT [see also Figs. 3(d) and 4]; subsequently the external field was decreased to $\mu_0 H_a = 53$ mT [Fig. 5(b)], 0 mT [remanent state, Fig. 5(c)], −53 mT [Fig. 5(d)], and −160 mT. The theoretical profiles were calculated from Eqs. (2) and (13). The measured profiles agree well with the theoretically calculated curves.

plied perpendicular to the sample surface and hence parallel to the c axis at a temperature $T = 30$ K. In Fig. 8 we applied external magnetic fields of $\mu_0 H_a = 53$ mT (a), 107 mT (b), 213 mT (c), and 0 mT [(d); this is the remanent state of Fig. 8(c)]. Figures 8(a) and 8(b) show that the vortices penetrate mainly in the middle of each edge since screening currents and stray fields are maximum there.[7,57,53] As already discussed in Sec. IV A, the flux distribution is disturbed by nonsuperconducting precipitates. The bridge visible in the upper part of the right sample edge is part of the voltage tap.

In Fig. 8(c) the sample is in the critical state; i.e., the Meissner currents have reached the critical current density everywhere in the sample. In the ideal critical state, the modulus of the current densities is constant $|j| = j_c$. Since j has to flow along the sample edges and has to satisfy the continuity equation, it will perform sharp bends which are imposed by the sample geometry.[58] This leads to the appearance of characteristic lines called d^+ lines. In our square geometry the current is forced to bend sharply at the diagonals where the d^+ lines are visible as dark lines. The cutoff lower left sample corner in Fig. 8 causes a perturbation of this ideal picture: Here, the sample has two corners which force the current to bend twice, and thus two d^+ lines are observed instead of one.

In addition to these d^+ lines, there are defects and edges where two regions with different critical current densities meet, e.g., at the sample edges or at boundaries separating two qualitatively different superconductors. At such boundaries the current lines have to bend sharply in order to satisfy the condition of continuous current flow. Again this leads to the appearance of characteristic lines at the loci where the value of the critical current density changes, which are labeled d^- lines.

Characteristic features of the d^+ and d^- lines are the following.

(1) Whereas the d^- lines occur at internal and external boundaries of the sample (local sample geometry), the d^+ lines form in homogeneous regions and reflect the shape of the sample.

(2) Flux lines cannot cross the d^+ lines since during increase or decrease of the applied magnetic field the flux motion is directed towards or away from the d^+ lines, respectively.

(3) The d^+ and the d^- lines do not change their position during lowering or reversing of the external magnetic field, although the magneto-optically detected intensities of the d^+ and d^- lines are reversed in the remanent state.

In thin type-II superconductors ($d \ll a$) these d^+ and d^- lines are clearly seen because of the logarithmic infinity of B_x at the sample surface.[53] In the remanent state [Fig. 8(d)] the negative flux at the sample edges is clearly visible. As yet, analytical or numerical solutions to the current distribution in the rectangular or square disk are not available.

C. Ring

The calculated penetration of flux into a ring in increasing $H_a(t)$ is presented in Fig. 9. The subsequent exit and new penetration of flux with opposite sign in decreasing field are shown in Fig. 10. In these simulations we choose an inner ring radius $r_0 = 0.6a$ (a = outer radius) and the current-voltage law $E(j) = (j/j_c)^{19} E_c$ with $j_c = j_0 = \text{const}$ and $E_c = E_0 = \text{const}$ as in Fig.

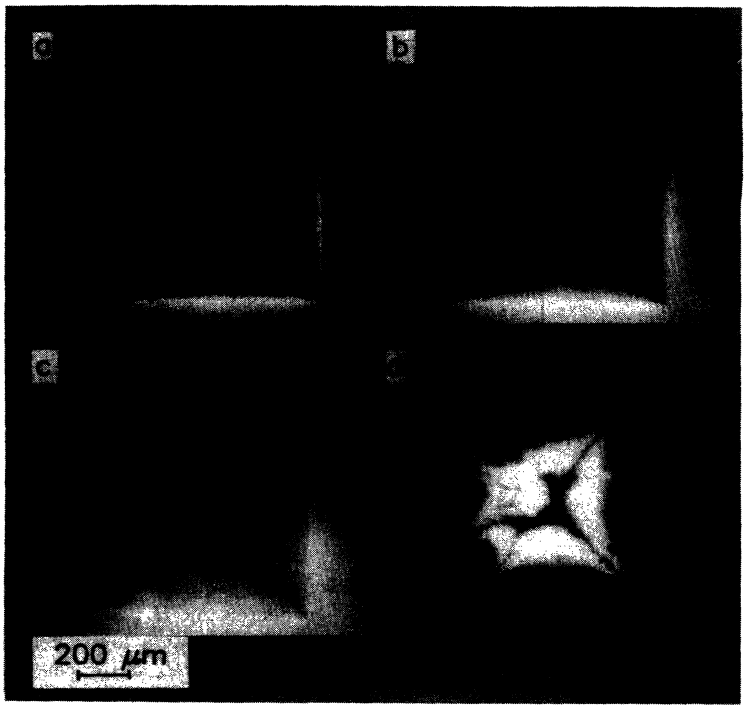

FIG. 8. Flux distributions of a nearly square patterned YBCO thin film (width 1 mm, thickness 300 nm). In this case an iron-garnet film was used as magneto-optical indicator. The external magnetic field $\mu_0 H_a$ is oriented perpendicular to the sample surface. (a) $\mu_0 H_a = 53$ mT, (b) $\mu_0 H_a = 107$ mT, (c) $\mu_0 H_a = 213$ mT, (d) $\mu_0 H_a = 0$ mT [remanent state of (c)].

1 (Bean model). The ramp rate was $|dH_a/dt| = 0.01$ in units $E_0/a\mu_0$. $H(r)$ and $J(r)$ are in units $J_0 = j_0 d$. With increasing H_a, flux penetrates the ring at both edges asymmetrically as described in Refs. 25 and 26: The ring carries a transport current induced by dH_a/dt and by H_a (because of conservation of the total flux inside a superconducting ring), and at the same time the ring has to shield H_a from its superconducting interior $r_0 \leq r \leq a$. Figures 9 and 10 show that this shielding is "currentlike" in the language of Ref. 25 since the current has the same sign at the inner and outer edges of the ring; see also Fig. 13.

In the virgin branch (H_a increased from zero, Fig. 9) full penetration of the ring is achieved in our simulation at $H_a \approx 0.4$. For $H_a < 0.4$ the total flux enclosed by the ring is zero; at $H_a = 0.4$ flux starts to penetrate into the hole of the ring, and the sheet current $J(r)$ saturates to an approximately constant value $0.8 j_c d$, from which the field profiles $H(r)$ follow by Eq. (4); cf. the discussion in Sec. II D. When H_a is increased further, $J(r)$ does not change and $H(r)$ keeps its shape but shifts up rigidly at the same rate as H_a; cf. Eq. (4).

Figure 10 shows the field and current profiles when H_a is decreased from +0.4 to −0.3. Saturation of the shielding current now occurs at a lower value of $|H_a| \approx 0.3$: One finds $J(r) \to -0.8 J_c$ in the decreasing branch, and $J(r) \to +0.8 J_c$ in the subsequent increasing branch when H_a is cycled. This general property of the virgin curve (which always runs below the full hysteresis loop) can be seen in the magnetization curve $M(H_a)$ of this ring in Fig. 11.

Figure 12 shows the flux distribution in a flat superconducting ring produced by sputtering off the central region of the other voltage measurement pad (cf. Sec. IV B). These pictures are taken at $T = 5$ K and $\mu_0 H_a = 11$ mT (a), 16 mT (b), 21 mT (c), and 42 mT (d). In Figs. 12(a)–12(c) magnetic flux has not yet penetrated from the outer sample edge into the central hole, whereas in Fig. 12(d) flux leaks into the hole through a defect, a region with lower j_c visible near the lower left sample corner. Due to this leak, a comparison of the measured data and the calculations is not possible for external magnetic fields exceeding the value of 21 mT at which this "weak spot" becomes transparent. This situation is illustrated in Fig. 13. Figure 13(a) shows the current flow and the magnetic field lines for an external field at which magnetic flux has not yet penetrated into the central hole since one still has a closed superconducting path in the

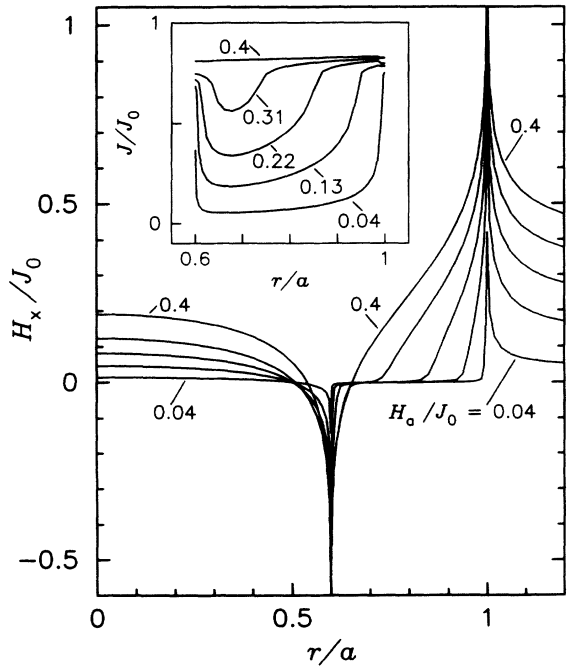

FIG. 9. Flux penetration into a superconducting ring with outer radius a and inner radius $r_0 = 0.6a$ and with current-voltage law $E(j) = (j/j_c)^{19} E_0$ where $j_c = j_0 = \text{const}$ and $E_0 = \text{const}$; cf. Fig. 1. Depicted are the perpendicular field $H(r)$ and the sheet current $J(r)$ (inset) in increasing applied field $H_a = 0.04, 0.13, 0.22, 0.31, 0.40$. H_a, H, and J are in units $J_0 = j_0 d$. The sweep rate was slower than in Figs. 1 and 2, $|dH_a/dt| = 0.01$ in units $E_0/a\mu_0$. At $H_a = 0.4$ the sheet current in the ring has saturated to an approximately constant value $\approx 0.8 j_c d$; with further increase of H_a the field profile keeps its shape and shifts rigidly up at the same rate as H_a.

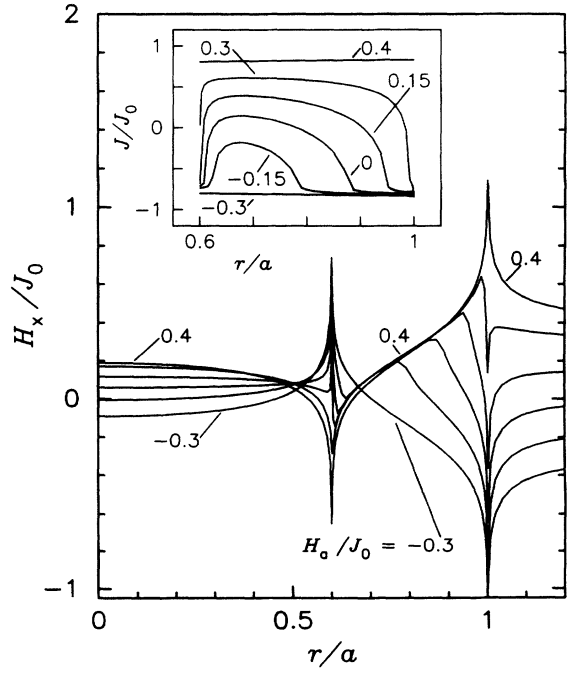

FIG. 10. As Fig. 9 but in decreasing applied field $H_a = 0.4, 0.3, 0.15, 0, -0.15, -0.3$. In decreasing H_a, and when H_a is cycled, the current density saturates at a lower field $|H_a| \approx 0.3$ than in the virgin branch when H_a is increased from zero.

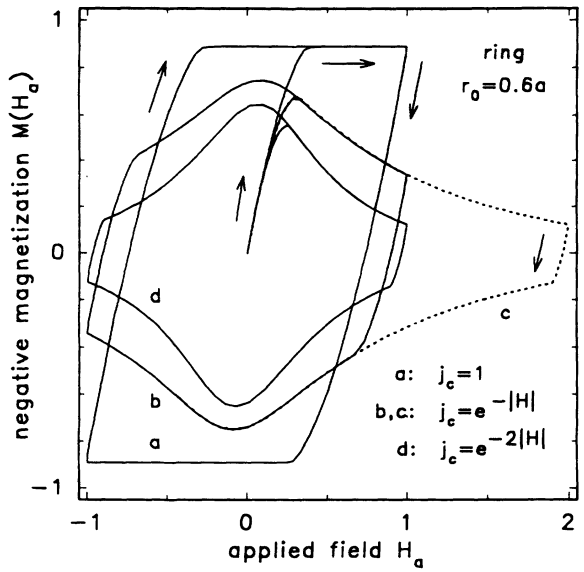

FIG. 11. Irreversibly magnetization curves $M(H_a)$ for the superconducting ring of Figs. 9 and 10. H_a and M are in units $J_0 = j_0 d$; $E(j) = (j/j_c)^{19} E_0$ was assumed; H_a was cycled with sweep rate $|H_a/dt| = 0.01$ in units $E_0/a\mu_0$. (a) As Figs. 9 and 10 ($j_c = j_0 = 1$, $|H_a| \leq 1$). (b) Field-dependent $j_c(H) = j_0 \exp(-|H|)$, $|H_a| \leq 1$. (c) As (b) but for larger amplitude $|H_a| \leq 2$. (d) Stronger field-dependent $j_c(H) = j_0 \exp(-2|H|)$.

ring. With increasing field the induced transport through the ring increases until the reduced critical current density in the weak spot is reached. This weak spot then enters the flux-flow state and allows flux lines to pass. Therefore, flux leaks from the outer sample edge into the central hole before the two penetrating flux fronts have met. As a consequence, the current flow and hence the magnetic field change as depicted in Fig. 13(b). The magnetic field generated by this current is presented as dashed lines, and the total field (the superposition of the homogeneous external field and the field of the circulating currents) is plotted as solid lines. The circular symbols indicate the direction and size of the currents. Note the enhanced B_x at the outer edge and the reversed B_x at the inner edge, with the absolute value of B_x being smaller at the inner edge than at the outer edge. This difference reflects itself in different light intensities at the inner and outer edges of the ring in Figs. 12(a)–12(c) and in the flux-density profiles in Fig. 14. The pictures in Fig. 12 were taken at a 90° polarizer-analyzer setting and, therefore, do not distinguish the positive and negative polarity of B_x. The different polarities of B_x in principle can be detected[56] by rotating the analyzer by some degrees, but this procedure reduces the contrast. In Fig. 13(a) equal numbers of field lines in both directions in the central hole indicate that the total flux Φ in this region is zero as long as magnetic flux has not penetrated from outside the ring.

As soon as magnetic flux has penetrated from the outer edge into the central hole of the ring, the currents flow antiparallel at the inner and outer edge ("fieldlike shielding") and thus the current-generated magnetic field is oriented along the external field at both sample edges, shielding the superconductor effectively from the external magnetic field. The unintentional presence of a weak spot (weak link or flux leak), therefore, allows one to observe both the "currentlike" and "fieldlike" shielding states predicted in Ref. 25 and occurring before and after the weak spot becomes transparent to flux motion, respectively. The effect of this weak spot is to limit the induced transport current through the ring by allowing

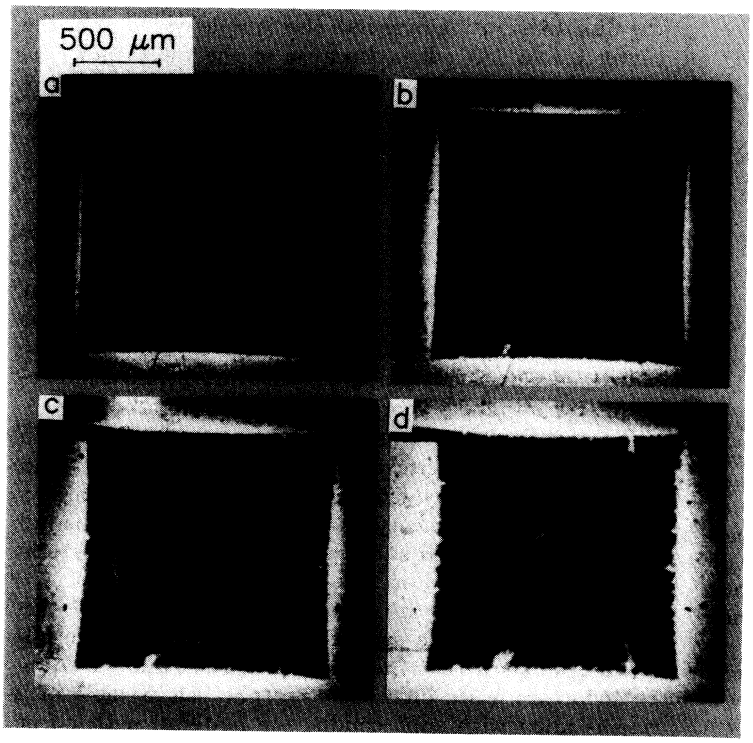

FIG. 12. Flux distribution of a ring-shaped YBCO thin film obtained at $T = 5$ K. (a) $\mu_0 H_a = 11$ mT, (b) $\mu_0 H_a = 16$ mT, (c) $\mu_0 H_a = 21$ mT, (d) $\mu_0 H_a = 42$ mT. Here, magnetic flux has penetrated into the inner hole at the defect structure which is visible near the lower left sample corner. The small bridge at the left sample edge is part of the voltage tap. For details see text.

flux to leak through. Without such a flux leak the total current is proportional to the applied field until the two flux fronts, entering with opposite polarity from the outer and inner edges, meet and start to annihilate each other.

The superposition of transport and shielding currents in the ring causes asymmetric flux penetration: More flux lines enter from the outer edge and penetrate deeper into the ring than from the inner edge. In the penetrated zones the maximum current density $\approx j_c$ flows. Consequently, the overshoot of B_x is larger at the outer edge than at the inner edge. The shape of the flux-density profiles $B_x(r)$ can be seen from Fig. 14. For external magnetic fields of $\mu_0 H_a = 11$ mT [corresponding to Fig. 12(a)] and 21 mT [cf. Fig. 12(c)] the profiles fit qualitatively well to the theoretical calculations plotted in

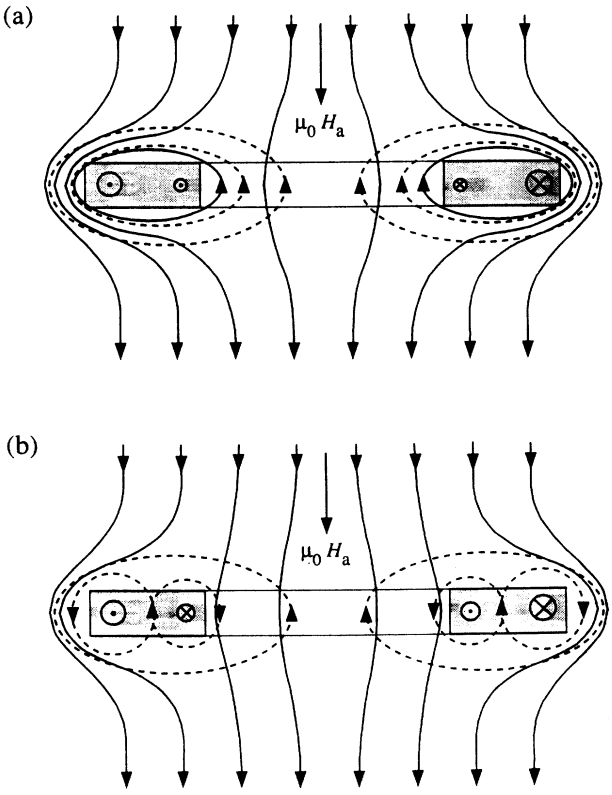

FIG. 13. Sketch of the magnetic field lines and the direction of current flow. The current-generated magnetic field is plotted as dashed lines, whereas the superposition of the homogeneous external magnetic field $\mu_0 H_a$ and current-generated field is drawn as solid lines. $\odot$ symbolizes the current which flows out of the drawing plane; $\otimes$ is the opposite flowing direction. (a) No flux has penetrated from outside the ring into the central hole. The equal numbers of field lines of opposite direction symbolizes $\Phi = 0$ in the central hole. (b) At one particular place the flux front has reached the inner edge of the ring and magnetic flux leaks into the central hole where now $\Phi > 0$.

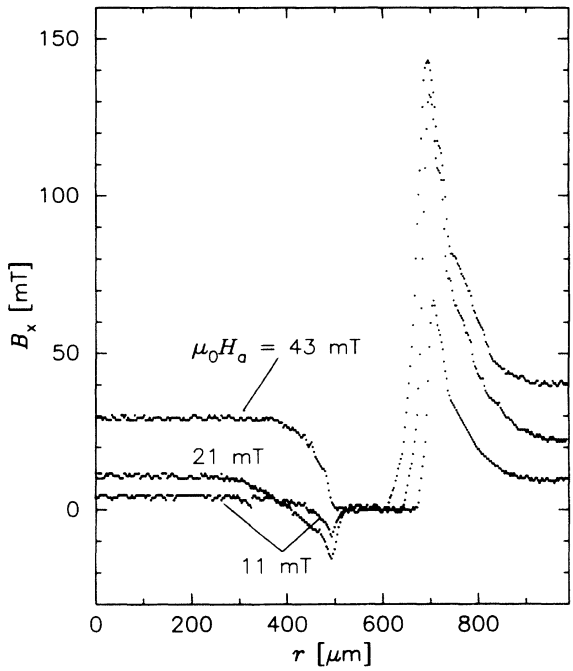

FIG. 14. Flux-density profiles measured at $T = 5$ K at $\mu_0 H_a = 11$ mT, 21 mT, and 42 mT. The profiles were obtained from experiments with higher magnification than in Fig. 12 and a polarizer-analyzer setting $\neq 90°$ in order to detect the different polarities of B_x at the sample edges. For details see text.

Fig. 9. In order to obtain better spatial resolution, the flux-density profiles were scanned from observations with higher magnification than in Fig. 12. The profiles show the flux distribution over half the sample width from the center to the left edge. Because of the weak spot, the flux penetration at fields $\mu_0 H_a > 21$ mT and the flux distributions obtained while decreasing and reversing the external magnetic field cannot be compared with our calculations. The profile measured at $\mu_0 H_a = 42$ mT and plotted in Fig. 14 shows that the flux distribution qualitatively goes over to the one of strip geometry since the weak spot limits the transport current through the ring. At fields $\mu_0 H_a > 42$ mT the flux-density profiles exhibit a pronounced positive overshoot at both sample edges as already shown in the pictures in Fig. 4. However, the above mentioned asymmetry of the flux penetration remains since the transport current is not exactly zero.

Since all known production techniques of YBCO thin films lead to an imperfect film growth, perfect grown and patterned samples which are required for a comparison of experiment and theory in the field range up to the full penetration field and subsequent decreasing and reversing the external field are not available.

In this section we discussed flux penetration and current distribution in a superconducting ring. In the following, we show that the flux penetration and shielding behavior are quite different when the central hole of a ring is filled with superconducting material with no or

very weak pinning or with a critical sheet current reduced by a factor of 2.

D. Inhomogeneous pinning

We now consider superconducting platelets with inhomogeneous J_c; one has irradiation-enhanced pinning near the edges and the other one a thinner central zone produced by sputtering it down to half thickness.

But before we compare our theoretical and experimental results we have to discuss a subtle point. The most salient feature of flux penetration into thin superconductors in increasing perpendicular field is the appearance of the supercurrent immediately over the whole sample surface (see Figs. 1 and 2). At the sample edges the value of this current is always highest, and if the superconductor is homogeneous, the front of the saturation of the current is always followed by flux penetration. But if the critical current density J_c in the edge zone is higher than in the center, the screening current can reach the lower J_c there *before* flux starts to penetrate. What will happen in this case? Two scenarios are conceivable:

(a) Zero (or reduced) sheet current J in the central zone may be forced by the nucleation of parallel vortices generated by J and oriented along the two flat surfaces in opposite direction. If these vortex-antivortex pairs are not pinned, they will move into the specimen and form vortex loops which do not violate the conservation of total flux in this central region; appropriate curvature of these vortices can then compensate the Meissner screening current. The resulting situation $J = 0$ is equivalent to the ring discussed in Sec. IV C. The magnetic field lines then close around the current-carrying edge zone.

(b) Alternatively, the sheet current J may exceed the J_c value in the central region if this stays completely free of perpendicular vortices, i.e., if the parallel vortices generated by the large sheet current are pinned. We will see that our experiments are consistent only with this latter assumption, expressed in our following calculations in the framework of the planar approximation by the condition $J_c = \infty$ in regions where $B_x = 0$.

For comparison, Figs. 15–18 show the calculated pen-

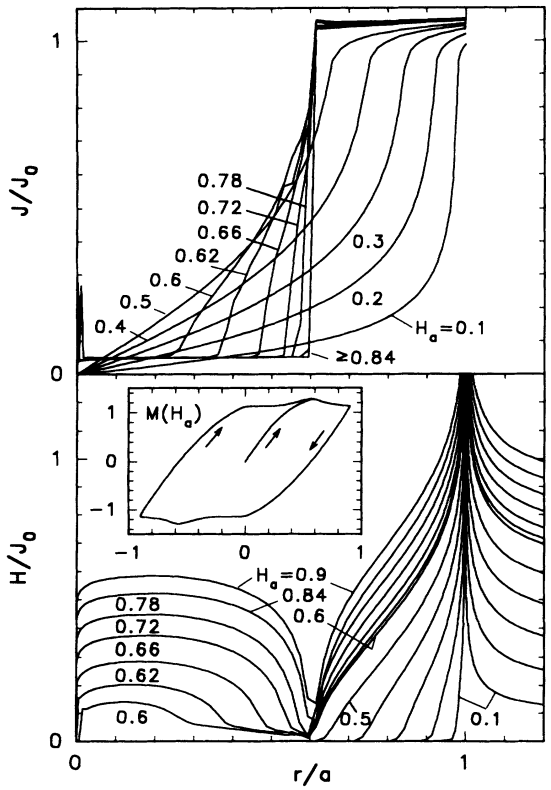

FIG. 15. Profiles of the sheet current $J(r)$ and perpendicular magnetic field $H(r)$ in a circular disk with radius a and thickness $d \ll a$ with irradiation-enhanced critical current density $j_c = j_0$ in the ring zone $r_0 \le r \le a$ and $j_c = j_{c1} = 0.05 j_0$ in the unirradiated central zone $0 \le r < r_0$. $r_0 = 0.6a$. J and H are in units $J_0 = j_0 d$. The current-voltage law was assumed as $E = (j/j_c)^{19} E_0$ with $j_c = j_c(r, |H|)$ chosen such that $j_c \gg j_0$ in regions where $|H| < 0.02$ (Meissner state). Increasing $H_a = 0.1$, 0.2, 0.3, 0.4, 0.5, 0.62, 0.66, 0.72, 0.78, 0.84, 0.9. The inset shows the corresponding magnetization curve.

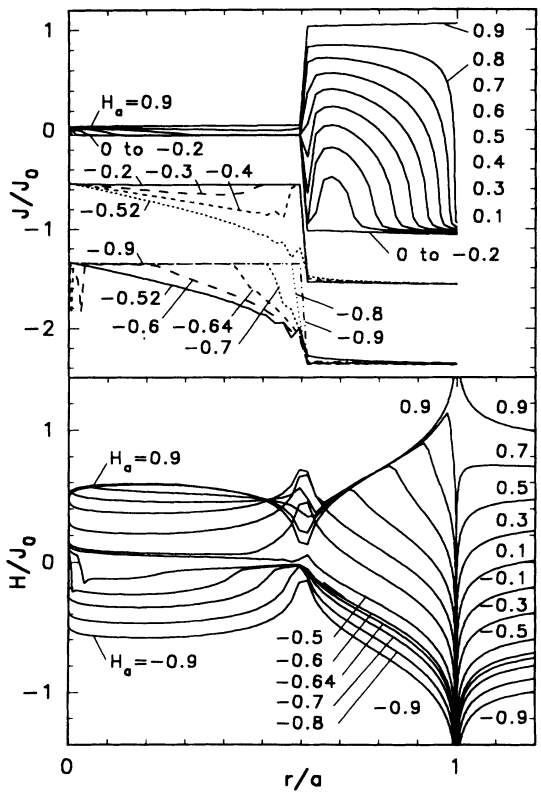

FIG. 16. The same as Fig. 15 but in decreasing H_a. $J(r)$ is shown for $H_a = 0.9, 0.8, \ldots, 0.1, 0, -0.1, -0.2$ (the last three curves coincide due to current saturation), $H_a = -0.2$, -0.3, -0.4, -0.52 (for clarity J is shifted down by 0.5), and $H_a = -0.52$, -0.6, -0.64, -0.7, -0.8, -0.9 (J shifted down by 1.3). $H(r)$ is shown for $H_a = 0.9, 0.7, \ldots, -0.3, -0.5, -0.6, -0.64, -0.7, -0.8, -0.9$.

etration and exit of flux in circular disks with critical sheet current $J_c = j_c d$ depending on the radius, namely, $J_c = J_0$ in the outer zone $r_0 = 0.6a \leq r \leq a$ and $J_c = J_{c1}$ in the central zone $0 \leq r < r_0$. We chose $J_{c1} = 0.05J_0$ in Figs. 15 and 16 and $J_{c1} = 0.5J_0$ in Figs. 17 and 18. This calculation [from Eqs. (4), (15), and (17)] for inhomogeneous pinning requires the additional assumption that the sheet current $J(r)$ should be *unlimited* in the flux-free zones, i.e., in regions which are in the Meissner state. This condition was achieved by formally multiplying the $J_c(r)$ entering our current-voltage law $E = (J/J_c)^{19}E_0$, by a factor which smoothly becomes very large for $|H|/J_0 \leq 0.02$. This choice yields a very stable numerical integration of Eq. (15). Note that in Fig. 16 the sheet current in decreasing H_a saturates to its steplike $J_c(r)$ *twice*: at $H_a = 0$ to -0.2 and at $H_a \leq -0.9$. This nonmonotonic behavior occurs when $H(r)$ passes through zero; in the regions with $H(r) = 0$, $J(r)$ can exceed $J_c(r)$ and will increase in order to shield H_a from the flux-free zone. By the same token $J(r)$ exhibits a narrow peak near $r = 0$ when $|H(r)| \leq 0.02$ there. These sharp peaks in $J(r)$ at the flux front are most clearly seen in Figs. 17 and 18; cf. also the peaks in Fig. 2. The height and shape of the peaks depend on the assumption how J_c goes to infinity when $|H|$ goes to zero. Note that in Fig. 15 one exactly has $H(r_0) = 0$ until flux penetration (or saturation of J) is completed. The penetrating flux lines thus have to move very fast through the boundary to the unirradiated zone.

Figure 19(a) shows the shape of the Bi2212 single crystal and the location of the absorber, the bright area in the sample center. In the sequence of Figs. 19(b)–19(h) flux distributions are presented at temperature $T = 50$ K for applied transverse fields of $\mu_0 H_a = 85$ mT (b), 107 mT (c), 128 mT (d), 149 mT (e), 171 mT (f), 213 mT (g), and 277 mT (h). The black lines indicate the sample edge. Figure 19(b) shows that the vortices penetrate into the superconductor only from the edges, mainly at the middle of each edge as described in Fig. 8. In Fig. 19(c) the flux front reaches the unirradiated area at the narrowest place of the irradiated belt [white arrow in the lower left corner in Fig. 19(c); see also Fig. 19(a)].

Now an interesting phenomenon occurs: Flux suddenly

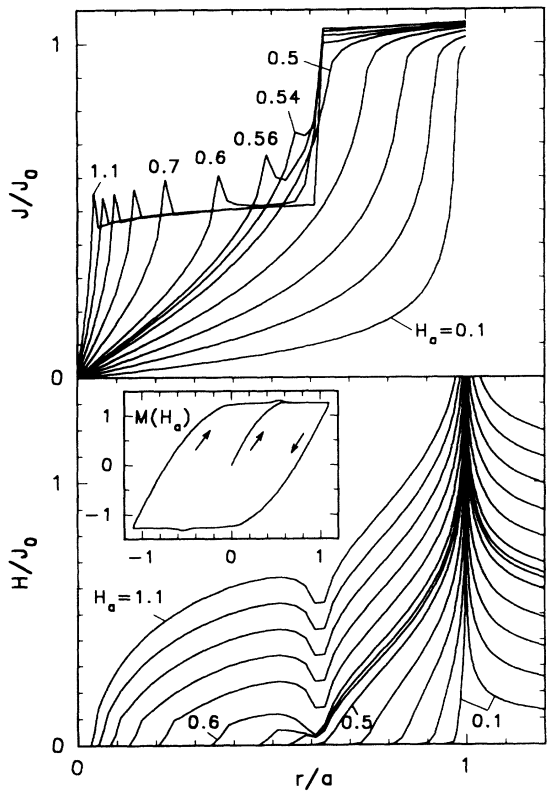

FIG. 17. Profiles of the sheet current $J(r)$ and perpendicular magnetic field $H(r)$ in a circular disk with radius a and original thickness $d \ll a$ with critical sheet current $J_c = j_c d = J_0$ in the ring zone $r_0 \leq r \leq a$ and $J_c = J_{c1} = 0.5J_0$ in the central zone $0 \leq r < r_0$ reduced by sputtering. $r_0 = 0.6a$. J and H are in units J_0. The current-voltage law was assumed as $E = (J/J_c)^{19}E_0$ with $J_c = J_c(r, |H|)$ chosen such that $J_c \gg J_0$ in regions where $|H| < 0.02$ (Meissner state). Increasing $H_a = 0.1, 0.2, \ldots, 0.5, 0.54, 0.6, 0.7, \ldots, 1.1$. The inset shows the corresponding magnetization curve.

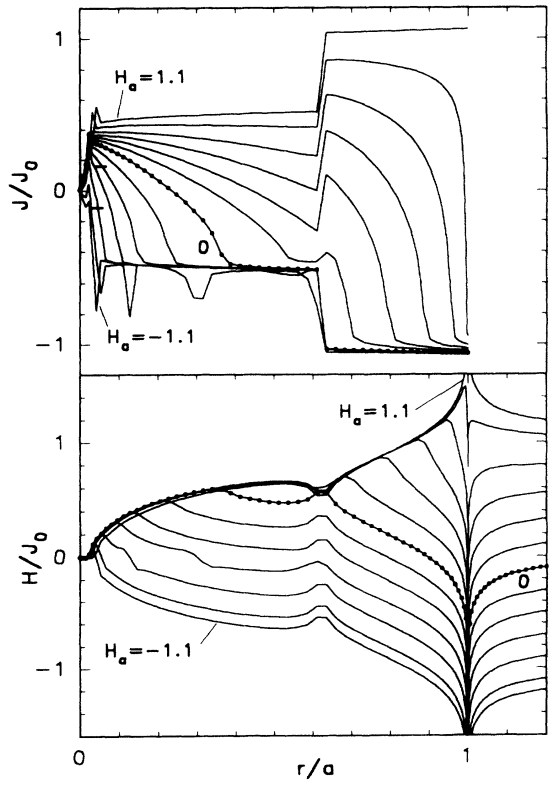

FIG. 18. The same as Fig. 17 but in decreasing H_a. $H_a = 1.1, 1, 0.8, 0.6, \ldots, 0, -0.2, \ldots, -1, 1.1$. The curves $H_a = 0$ (remanent state) are marked by dots.

appears in the center of the Meissner area (white arrow in the sample center). At the same time, the motion of the flux front from the sample edges slows down and the magnetization is dominated by the spread of flux from the center. Since vortices cannot nucleate at the sample center, they have to cross the Meissner area being driven to the center by screening currents which are much higher ("overcritical") than the j_c in this unirradiated region, Figs. 19(d)–19(f). This situation is analogous to the penetration of flux bundles over an edge barrier observed in type-I superconductors[59] and recently in Bi2212 single crystals.[60] In Figs. 19(g) and 19(h) the unirradiated part

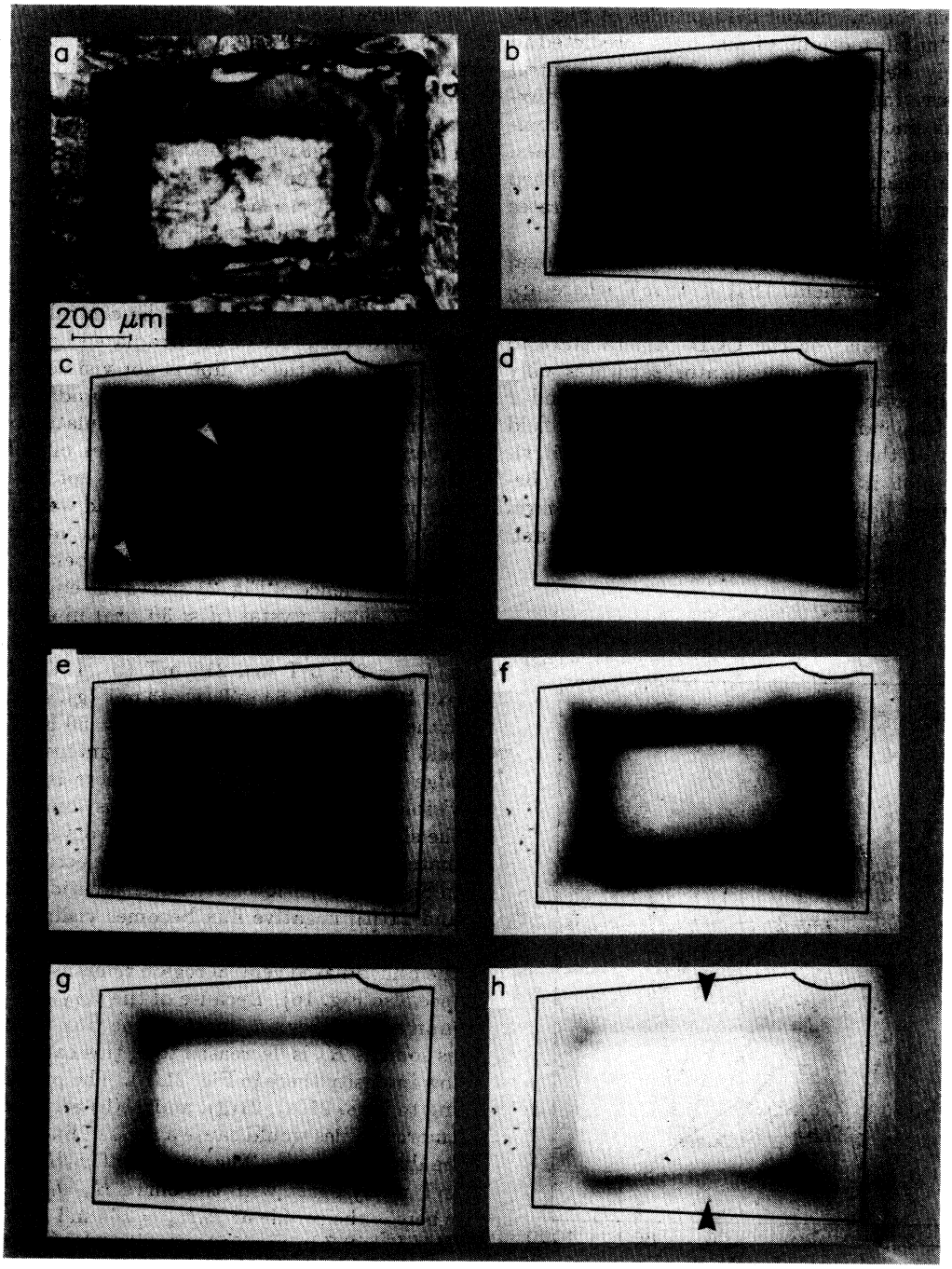

FIG. 19. (a) Shape of the irradiated Bi2212 single crystal. The absorber is visible as bright region in the sample center. (b) Flux distribution at $T = 50$ K in a transverse magnetic field of $\mu_0 H_a = 85$ mT. (c) $\mu_0 H_a = 107$ mT. The flux starts to penetrate the unirradiated part of the sample at the narrowest place of the irradiated belt (white arrow in the lower left corner) and piles up in the sample center as indicated by the other white arrow. (d) $\mu_0 H_a = 128$ mT. (e) $\mu_0 H_a = 149$ mT. (f) $\mu_0 H_a = 171$ mT. (g) $\mu_0 H_a = 213$ mT. (h) $\mu_0 H_a = 277$ mT.

of the sample is completely filled with flux lines and the flux front has moved from the sample edge to the inner edge of the irradiated belt. In the irradiated belt only the critical current flows and further increase of H_a does not change the shape of the flux-density profiles but shifts them rigidly at the same rate as H_a.

The appearance and growth of the magnetic flux in the sample center is clearly seen in the flux-density profiles measured across the sample, Fig. 20. These profiles nicely agree with the calculated field profiles of Fig. 15. Moreover, the "uphill motion" of flux lines, predicted in Ref. 25, is clearly seen: During the growth of the central flux heap the arriving flux lines move against the flux-density gradient since the driving current in this geometry is caused mainly by the curvature of the flux lines. Notice that the measured profiles do not show a sharp cusp at the sample edge since the garnet film saturates at a magnetic field of about 200 mT.

In general, the light intensity I is roughly proportional to $|B_x|$ except for small fields $|B_x| < 10\,\mathrm{mT}$ where approximately $I \sim B_x^2$, and for $|B_x| > 200\,\mathrm{mT}$ where the garnet indicator and/or the CCD camera start to saturate (the EuSe thin film indicator saturates only above 2 T). The exact relationship between B_x and I is not known (depending, e.g., on the magnetic field at the position of the CDD camera). For optimal visualization we plot in Figs. 20, 22, 24, and 28 below the measured light intensity profiles in the form $\tilde{B}_x = \mathrm{const} \times I(|B_x|) \times \mathrm{sign}(B_x)$ with arbitrary constant.

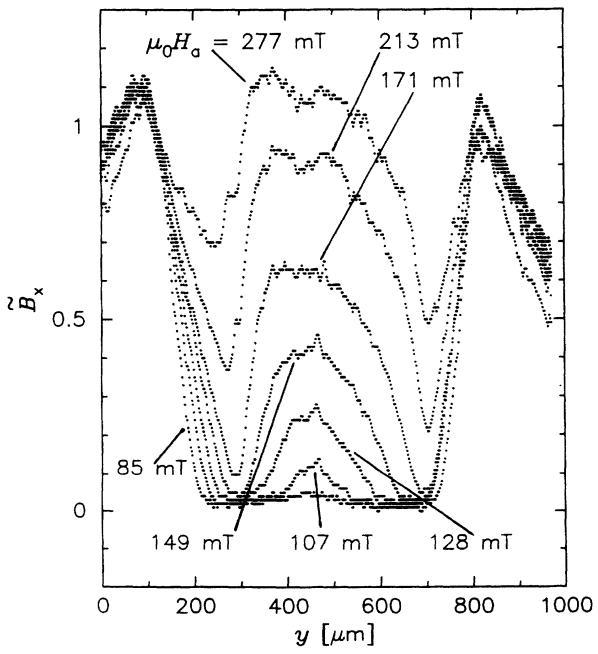

FIG. 20. Flux-density profiles taken from Figs. 19(b)–19(h) along the line indicated by two arrows in Fig. 19(h). The measured field profiles nicely agree with the calculated ones shown in Fig. 15.

At this point we will discuss interesting features of flux line motion within the framework of d lines (see Sec. IV B and Ref. 53). In the unirradiated area d^+ lines which could be expected running from the corners to the center along the bisection lines do not appear and in the irradiated region only a short d^+ line exists running from the sample corners to the boundary between the two regions. This is due to the fact that at $T = 50$ K the unirradiated part of the sample is above the depinning line where the critical current is zero. When the flux front has reached the d^- line at the narrowest place of the outer belt, which separates the irradiated from the unirradiated zone, the vortices which are driven to the center of the unirradiated zone and pile up there to form a new flux front which moves from the center towards the d^- line as the unirradiated zone is filled with flux lines. This flux front then penetrates into the irradiated belt and causes "fieldlike" shielding of a strip as discussed for the ring (see Sec. IV C). With further increase of the external field a d^+ line is formed in the irradiated zone near the inner boundary to the central region except at the narrowest place of the irradiated belt, Fig. 19(h). At the lower edge the d^+ line is not visible because it is too close to the d^- line at the inner boundary. The observed experimental situation may be simulated by a strip with enhanced pinning in its edge zones of different widths. However, such calculations would not give new insight. In our experiments the external field was increased to the value where flux starts to penetrate markably from the inner boundary into the irradiated belt.

The sequence of Fig. 21 shows the edge-zone-irradiated Bi2212 single crystal ($d \approx 30$ μm) in external magnetic field decreasing from $\mu_0 H_0 = 277$ mT [see Fig. 19(h)] to $\mu_0 H_a = 256$ mT (a), 213 mT (b), 177 mT (c), 128 mT (d), 107 mT (e), 64 mT (f), 43 mT (g), and 0 mT [(h), remanent state of Fig. 19 (h)] at $T = 50$ K. The further the field is decreased the lower is the intensity at the sample edge (black frame) as long as there is no negative flux visible, Figs. 21(a)–21(f). This is due to the switch of the sheet current J (see Fig. 16) from $+J_c$ to $-J_c$ immediately when the external field is decreased as discussed in Sec. IV A. At low external magnetic fields [Figs. 21(g) and 21(h)] negative flux becomes visible as bright zones at the sample edge. In Figs. 21(a)–21(f) the intensity of the unirradiated central region remains nearly unchanged (see also Fig. 16). Because of the very low pinning in the unirradiated region, most of the flux immediately exits as soon as H_a is decreased to 0; this can be seen from the low intensity there in Fig. 21(h). The profiles corresponding to Figs. 21(a), 21(g), and 21(h) are plotted in Fig. 22 (more profiles would cause a mess of lines which could not be distinguished). The profiles of $\mu_0 H_a = 43$ mT and 0 mT nicely agree with the curve $H_a/J_0 = 0.1$ in Fig. 16, whereas the profile at $\mu_0 H_a = 256$ mT (corresponding to $H_a/J_0 = 0.7$ in Fig. 16) exhibits a higher intensity in the unirradiated zone than at the sample edges. The step of $J = 0$ to $J = -J_c$ causes a negative logarithmic infinity of B_x at the sample edge; see Sec. IV A. The slightly smeared step of $J(r)$ from $J = -J_c$ to $J = +J_c$ leads to a finite positive overshoot of B_x near the sample edges. Due to the thickness $d \approx 3.5$ μm of the iron-garnet indi-

cator, both effects cannot be spatially resolved and their superposition yields a reduced intensity.

Figure 23 shows the flux distribution of the edge-zone-irradiated Bi2212 single crystal in increasing reversed field $\mu_0 H_a = -21$ mT (a), -85 mT (b), -100 mT (c), -128 mT (d), -149 mT (e), -171 mT (f), -213 (g), and -277 mT (h), which was applied to the remanent state of $\mu_0 H_0 = 277$ mT [see Figs. 19(h) and 21(h)]. In Figs. 23(a) and 23(b) negative flux generated by the external magnetic field penetrates the sample from the edges and through the narrowest place of the irradiated belt. In Fig. 23(c) negative flux has started to penetrate the unirradiated central region similarly as in Fig. 19 but at lower $|H_a|$. The reasons for this behavior will be discussed later

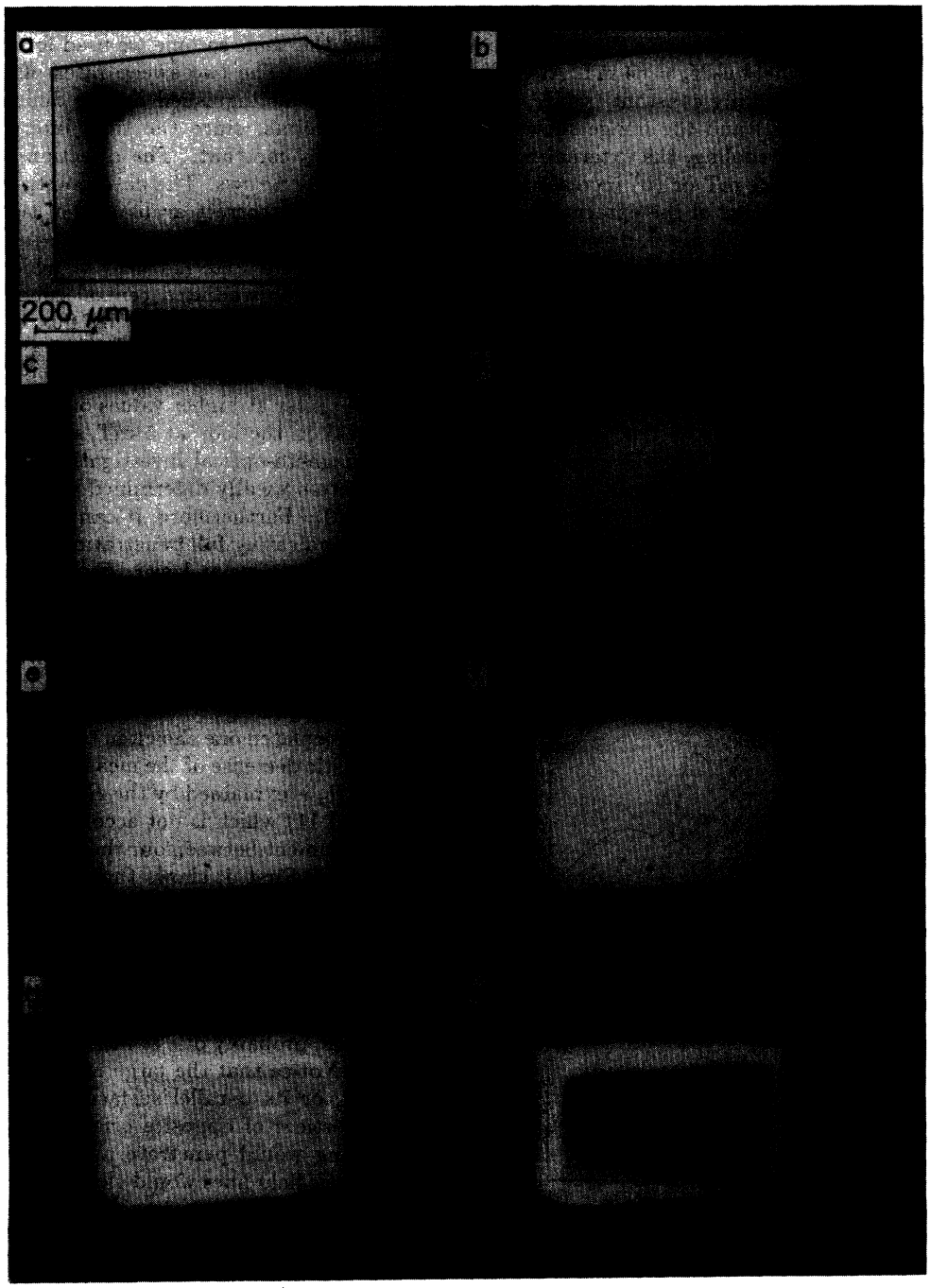

FIG. 21. Flux distributions of the same Bi2212 single crystal at $T = 50$ K. In these experiments the external magnetic field is decreased from $\mu_0 H_0 = 277$ mT to various external fields $\mu_0 H_a$. (a) $\mu_0 H_a = 256$ mT, (b) $\mu_0 H_a = 213$ mT, (c) $\mu_0 H_a = 177$ mT, (d) $\mu_0 H_a = 128$ mT, (e) $\mu_0 H_a = 107$ mT, (f) $\mu_0 H_a = 64$ mT, (g) $\mu_0 H_a = 43$ mT, (h) $\mu_0 H_a = 0$ mT (remanent state).

in this section when we consider the measured magnetization curve. Figures 23(d)–23(h) show the same flux penetration behavior as discussed for virgin magnetization [see Fig. 19(d)–19(h)]; i.e., in the central unirradiated zone the flux lines move against the gradient and overcritical currents flow in the flux-free regions there. The profiles corresponding to Figs. 23(a) and 23(c)–23(h) are plotted in Fig. 24. The measured profiles agree qualitatively well with the calculated curves in Fig. 16.

To demonstrate the existence of overcritical currents in flux-free regions field-cooling experiments were performed on the edge-zone-irradiated Bi2212 single crystal. Figure 25 shows the sample cooled down to $T = 50$ K in an applied external magnetic field $\mu_0 H_a = 64$ mT. At this moment the flux density is spatially constant ($\approx H_a$; no Meissner expulsion is observed) and the image shows a uniform grey area. After field cooling, the external field was (a) decreased to $\mu_0 H_a = 21$ mT or (b) increased to $\mu_0 H_a = 107$ mT. After this change of the external field, vortices in the central region start to move, driven by the induced current. This motion should be the same as after zero-field cooling followed by the same increment of H_a; compare Figs. 25(a) and 25(b) with Fig. 19(b), where an even larger field increment does not affect the flux distribution inside the irradiated belt. In the presence of unpinned vortices in the unirradiated part (such that an overcritical current is not possible) the flux motion induced by the increment of H_a is nearly the same as in the ring discussed in Sec. IV C. When H_a is *decreased*, the inner vortices move to the irradiated belt and concentrate at its inner boundary; see the bright line in Fig. 25(a). When the field is *increased*, vortices move to the center leaving behind a narrow dark zone with $H_x = 0$ at the inner boundary of the belt. This zone with $H_x = 0$ is also clearly seen in our calculations. Thus, the unirradiated region at $T = 50$ K exhibits extremely low pinning, even for single perpendicular vortices; very low current suffices to move the perpendicular vortices, and a high "overcritical" nondissipative supercurrent is possible after these vortices are swept away.

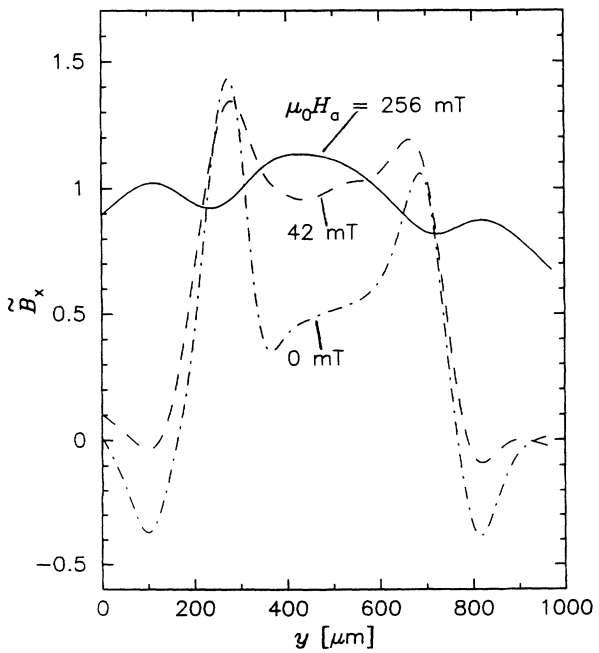

FIG. 22. Measured flux-density profiles after application of an external magnetic field of $\mu_0 H_0 = 277$ mT; subsequently the external field was decreased to the indicated values. For details see text.

Figure 26 shows magnetization curves measured at $T = 50$ K on the *same* sample we used for magneto-optical investigations. The two sweep rates of 5 mT/s and 20 mT/s can be distinguished by the different densities of measuring points, since the time interval between the data points is constant. The direction of measurement is indicated by arrows. The data points near $H_a \approx 0$ are omitted, since a correct evaluation of the torque data is not possible here; see Eq. (18). The peak of the virgin branch marks the external field at which flux starts to penetrate the unirradiated central zone. At the higher sweep rate J_c is less reduced by flux creep effects, resulting in a larger hysteresis loop; cf. also Figs. 1 and 2. Therefore, at the faster sweep rate of 20 mT/s flux penetrates the center at higher values of H_a. The value of H_a at this peak in the loop at 5 mT/s (the sweep rate used for our magneto-optical investigations) agrees well with the magneto-optically determined value $\mu_0 H_a = 107$ mT (see Fig. 19). Furthermore, it can be seen that the second peak, indicating full penetration of negative flux (see also Fig. 23), occurs at lower $|H_a|$. The reasons for this behavior are flux creep effects which reduce J_c and facilitate flux penetration [see Eq. (8)], and the negative flux which has penetrated the sample already in the remanent state.

The measured magnetization curves qualitatively agree with the calculated one shown in the inset of Fig. 15. The characteristic decrease of the measured magnetic moment at higher H_a is explained by the H_a dependence of J_c (see Figs. 2 and 11) which is not accounted for in Fig. 15.

The agreement between our theory and the experiment is not trivial. First, it shows that a theory which considers only the averaged components of j and E parallel to a specimen of finite thickness is sufficient. Second, this agreement also means that in the unirradiated zone pinning is weak only for *perpendicular* flux, but it is strong enough to prevent *parallel* flux lines to penetrate from the flat surfaces, probably due to intrinsic pinning by the Cu-O layers. Notice that the large Meissner screening sheet current J, or its parallel surface field $\pm J/2$, generates parallel vortices of opposite orientation, which without this pinning would penetrate and annihilate such that the magnetic field lines would close around the irradiated frame as with a current-carrying loop. This would cause a negative cusp of H_x at the inner edge of the irradiated zone, which is not observed in our experiments.

A different pattern of flux distribution is observed when the critical current in the inner region is about half the value of the outer zone. This situation is realized in a Bi2212 single crystal whose central zone was

thinned down to about half thickness. Figure 27 shows the obtained flux distributions in increasing field $\mu_0 H_a$ = 384 mT (a), 427 mT (b), 469 mT (c), 512 mT (d), 534 mT (e), and the remanent state of 534 mT (f) at T = 20 K. In the sequence of Figs. 27(b)–27(e), the flux front speeds up when it has reached the thinned central region. Consider the first vortex that reaches the thinned zone: It meets overcritical current and thus is driven quickly through this region to the place where the screening current equals the critical current there. From this place

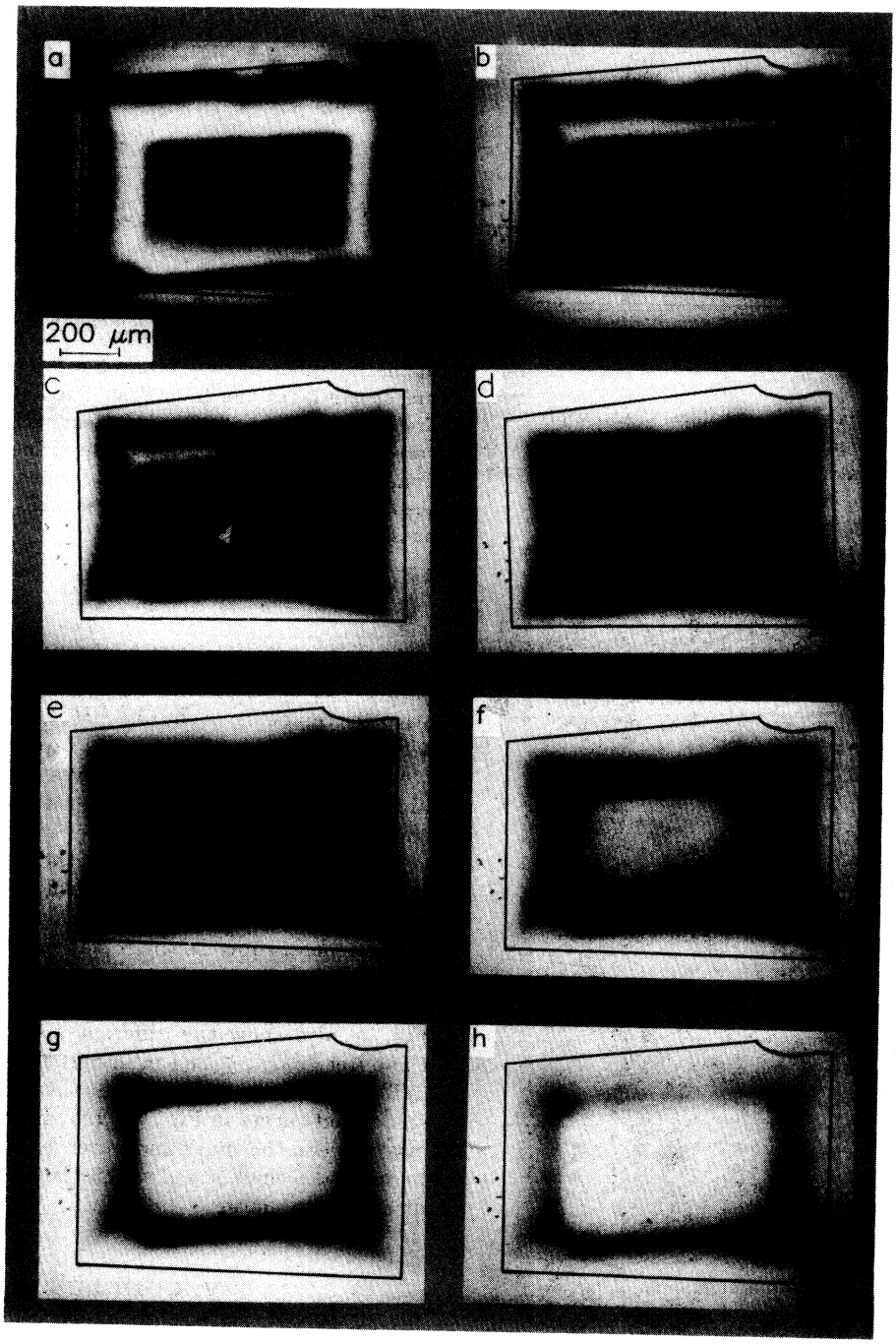

FIG. 23. Flux distribution of the edge-zone-irradiated Bi2212 single crystal when applying a reversed field H_a to the remanent state. (a) $\mu_0 H_a = -21$ mT, (b) $\mu_0 H_a = -85$ mT, (c) $\mu_0 H_a = -100$ mT; here negative flux has started to penetrate the unirradiated zone (white arrow). (d) $\mu_0 H_a = -128$ mT, (e) $\mu_0 H_a = -149$ mT, (f) $\mu_0 H_a = -171$ mT, (g) $\mu_0 H_a = -213$ mT, (h) $\mu_0 H_a = -277$ mT.

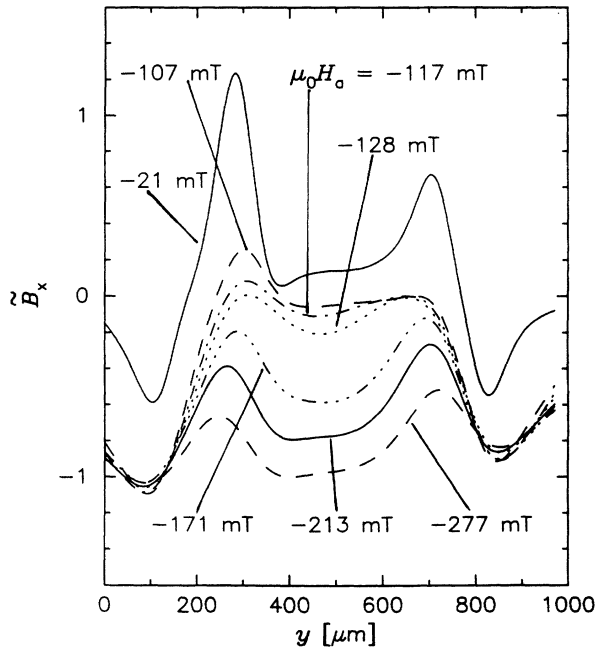

FIG. 24. Measured flux-density profiles when applying a reversed field to the remanent state of $\mu_0 H_0 = 277$ mT. The profiles agree qualitatively well with the calculated ones shown in Fig. 16.

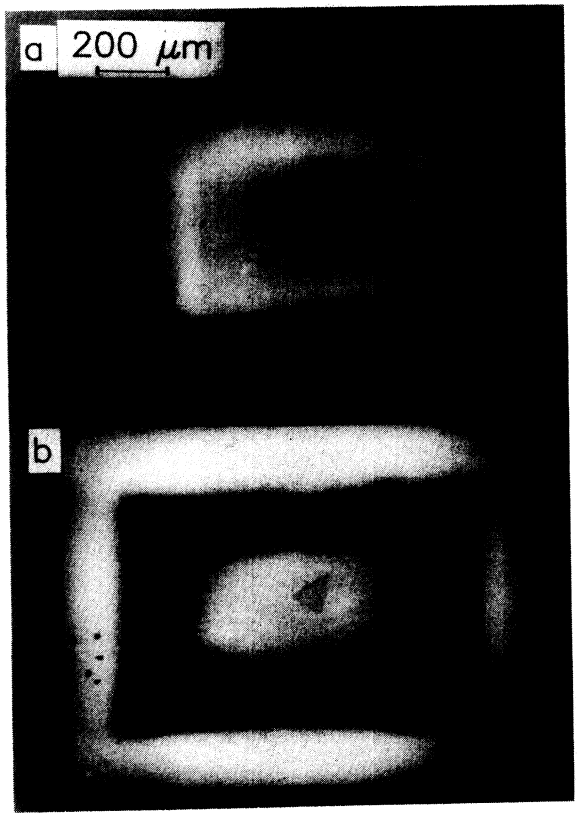

FIG. 25. Field-cooling experiments performed on the edge-zone-irradiated Bi2212 single crystal. The sample was cooled down to $T = 50$ K in an applied field of $\mu_0 H_a = 64$ mT. (a) $\mu_0 H_a = 21$ mT, (b) $\mu_0 H_a = 107$ mT. For details see text.

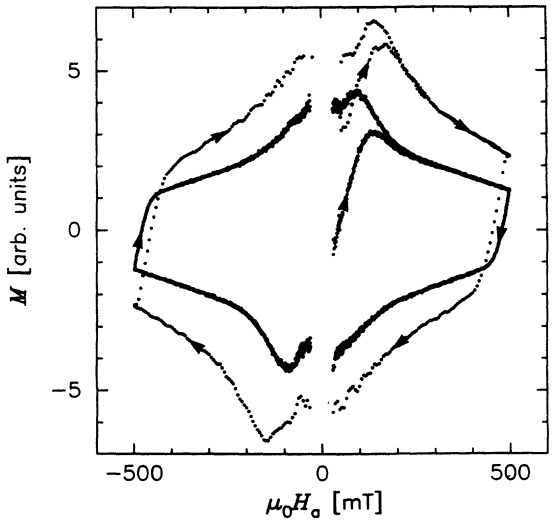

FIG. 26. Magnetization curves of the edge-zone-irradiated Bi2212 single crystal at $T = 50$. The loops were measured at the two different sweep rates 5 mT/s (the measured points are denser here) and 20 mT/s. The data points at $H_a \approx 0$ are omitted, since the measurement technique does not give correct values here. In this plot the influence of flux creep, inhomogeneous pinning, and the H_a dependence of J_c is clearly seen. The measured curves agree well with the theoretical ones.

[which can be calculated analytically from Eq. (6) for a strip by replacing J_c by J_{c1}, $J(y)$ by J_{c2}, and b by r_0], a flux front starts to penetrate rapidly towards the center, and a second flux front moves to the edge zone with higher J_c where it meets the front penetrating from the edge.

This behavior is similar to the edge-zone-irradiated Bi2212 single crystal where the flux penetration of the inner region proceeds from the center since here $J_{c2} = 0$ in the central zone. In the remanent state [Fig. 27(f)] the different penetration depths in the inner and outer region are clearly visible. The measured flux-density profiles in Fig. 28 also show the different penetration depths into the outer ($\mu_0 H_a \leq 384$ mT) and the inner ($\mu_0 H_a \geq 427$ mT) region. These profiles qualitatively agree with the calculated curves in Fig. 17. The dip of B_x at the boundary between the inner and outer area cannot be resolved because the thickness $d \approx 3.5$ μm of the iron-garnet indicator is too large.

V. CONCLUSION

In this paper we have investigated by theory and experiment the penetration and exit of magnetic flux, and the circulating sheet current induced by a cycled applied field $H_a(t)$, in superconducting platelets, strips, and rings with uniform pinning, and in platelets with strong and

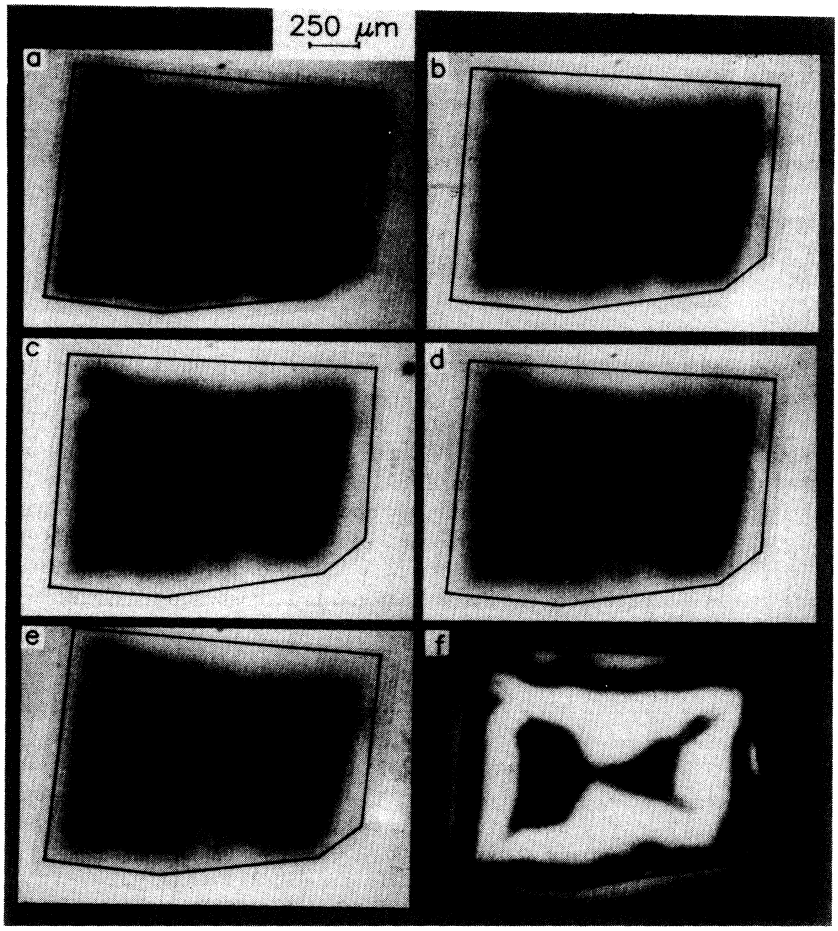

FIG. 27. Flux distributions in a Bi2212 single crystal with thinned central region at T = 20 K. (a) $\mu_0 H_a$ = 384 mT; the white frame indicates the thinned-down region. (b) $\mu_0 H_a$ = 427 mT, (c) $\mu_0 H_a$ = 469 mT, (d) $\mu_0 H_a$ = 513 mT, (e) $\mu_0 H_a$ = 534 mT, (f) remanent state of (e).

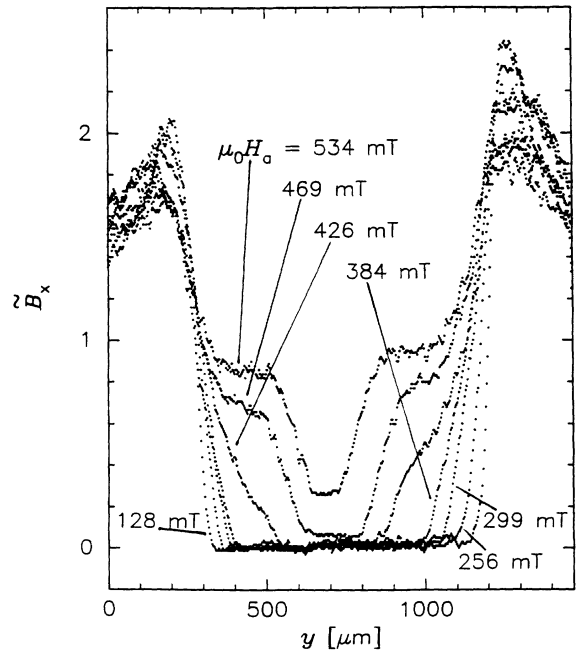

FIG. 28. Flux-density profiles of the Bi2212 single crystal shown in Fig. 27. The flux penetration in two steps is clearly visible. The profiles nicely agree with the theoretical curves plotted in Fig. 17.

weak inhomogeneities in the critical sheet current generated by heavy-ion irradiation of the edge zone or by sputtering down the central region. Our theoretical description of flux motion in perpendicular geometry is based on classical electrodynamics in planar approximation, assuming $B_x = \mu_0 H_x$ (or $H_{c1} = 0$) and a strongly nonlinear resistivity [Eq. (17)] with a space- and field-dependent critical sheet current $J_c(|H_x|, \mathbf{r}) = j_c(|H_x|, \mathbf{r}) \cdot d(\mathbf{r})$. If the time dependence is not crucial, i.e., in quasistatic problems, our theory applies even when the current density $\mathbf{j}(\mathbf{r})$ varies over the specimen thickness, e.g., if this is in a longitudinal Bean critical state induced by the sheet current; in this case the sheet current J is j integrated over the thickness. In fact, our planar approximation with the condition $J_c = \infty$ for $H_x = 0$ contains information about the anisotropy of the critical current density since it makes the assumption that the parallel vortices generated by the screening current in the Meissner regions with $H_x = 0$ are strongly pinned even when perpendicular vortices in the same region would be weakly pinned or even be mobile due to thermal depinning.

We compare our dynamic theory with the recently obtained[22–26] analytical solutions for the field profiles $H(\mathbf{r})$ and the sheet current profiles $J(\mathbf{r})$ in the static Bean model of flat superconductors in perpendicular field. In addition, the theoretical profiles in a ring confirm the extension[25,26] of these analytical solutions to the presence of both a transport current (induced in the ring)

and an external field. Magneto-optically determined flux-density profiles of a strip in increasing and decreasing field were compared with calculated ones taking into account the finite thickness of the magneto-optical detector. A very good quantitative agreement between theory and experiment is obtained for strip geometry without using fitting procedures.

An important theoretical result is that the logarithmic infinities of B_x and the vertical slope of the flux front are not removed when j_c is allowed to depend on B.

On our ring-shaped thin film with $d = 300$ nm, we observe the qualitatively different "fieldlike" and "currentlike" shielding states in which the current-generated field at the sample edges is oriented along or against the external field.

On an edge-zone-irradiated Bi2212 single crystal ($d \approx 30$ μm) the existence of overcritical currents in the absence of magnetic flux and the predicted "uphill" motion[25] of flux lines was studied.

The experimentally determined flux-density profiles of all our samples nicely agree with the calculated ones. Thus, our planar approximation and the assumption of a nonlinear current-voltage law and of $H_{c1} = 0$ yields an adequate description of even complicated flux distributions in inhomogeneous superconductors. Our specially designed inhomogeneous superconductors allowed us to find the additional and nontrivial assumption $j_c = \infty$ for $B_x = 0$, which is required for a correct description of flux penetration in the presence of inhomogeneous pinning.

ACKNOWLEDGMENTS

We wish to thank Professor H. Kronmüller for his constant interest in this work, T. W. Li (Leiden University), A. A. Menovsky (University of Amsterdam), and the Dutch FOM (ALMOS) for the Bi2212 single crystals, H.-U. Habermeier (MPI für Festkörperforschung) for preparation of the thin films, B. Ludescher (MPI für Metallforschung) for thinning down the Bi2212 single crystals, and A. J. J. van Dalen (Vrije Universiteit Amsterdam) for his collaboration. M.V.I. acknowledges financial support from the Swiss National foundation under Grant No. PNR 4030-32794.

[1] H. Kirchner, Phys. Lett. **26A**, 651 (1969).
[2] R. P. Huebener, *Magnetic Flux Structures in Superconductors* (Springer, New York, 1979).
[3] N. Moser, M. R. Koblischka, B. Gegenheimer, H. Kronmüller, and H. Theuss, Physica (Amsterdam) C **159**, 117 (1989).
[4] A. A. Polyanskii, V. K. Vlasko-Vlasov, M. V. Indenbom, and V. I. Nikitenko, Sov. Tech. Phys. Lett. **15**, 872 (1989).
[5] A. Forkl, T. Dragon, and H. Kronmüller, J. Appl. Phys. **67**, 3047 (1990).
[6] Th. Schuster, M. R. Koblischka, N. Moser, B. Ludescher, and H. Kronmüller, Cryogenics **31**, 811 (1991).
[7] P. Brüll, D. Kirchgässner, and P. Leiderer, Physica (Amsterdam) C **182**, 339 (1991).
[8] L. A. Dorosinskii, M. V. Indenbom, V. I. Nikitenko, Yu. A. Ossip'yan, A. A. Polyanskii, and V. K. Vlasko-Vlasov, Physica (Amsterdam) C **203**, 149 (1992).
[9] P. Leiderer, P. Brüll, T. Klumpp, and B. Stritzker, Physica B **165 & 166**, 1387 (1990); P. Brüll, R. Steinke, P. Leiderer, J. Schubert, W. Zander, and B. Strizker, Supercond. Sci. Technol. **5**, 299 (1992).
[10] D. A. Brawner and N. P. Ong, J. Appl. Phys. **73**, 3890 (1993).
[11] D. A. Brawner, A. Schilling, H. R. Ott, R. J. Haug, K. Ploog, and K. von Klitzing, Phys. Rev. Lett. **71**, 785 (1993).
[12] C. P. Bean, Rev. Mod. Phys. **36**, 31 (1964); J. Appl. Phys. **41**, 2482 (1970); A. M. Campbell and J. Evetts, Adv. Phys. **21**, 199 (1972).
[13] A. Gurevich and H. Küpfer, Phys. Rev. B **48**, 6477 (1993).
[14] J. R. Clem and Zh. Hao, Phys. Rev. B **48**, 13 774 (1993).
[15] D. J. Frankel, J. Appl. Phys. **50**, 5402 (1979).
[16] M. Däumling and D. C. Larbalestier, Phys. Rev. B **40**, 9350 (1989).
[17] L. W. Conner and A. P. Malozemoff, Phys. Rev. B **43**, 402 (1991).
[18] H. Theuss, A. Forkl, and H. Kronmüller, Physica (Amsterdam) C **190**, 345 (1992).
[19] V. K. Vlasko-Vlasov, L. A. Dorosinskii, M. V. Indenbom, V. I. Nikitenko, A. A. Polyanskii, and R. L. Prozorov, Superconductivity **6**, 705 (1993).
[20] S. Senoussi, J. Phys. III (France) **2**, 1041 (1992).
[21] A. Forkl, Phys. Scr. T **49**, 148 (1993); A. Forkl and H. Kronmüller, Physica (Amsterdam) C **228**, 1 (1994).
[22] P. N. Mikheenko and Yu. E. Kuzovlev, Physica C **204**, 229 (1993).
[23] J. Zhu, J. Mester, J. Lockhart, and J. Turneaure, Physica (Amsterdam) C **212**, 216 (1993).
[24] E. H. Brandt, M. Indenbom, and A. Forkl, Europhys. Lett. **22**, 735 (1993).
[25] E. H. Brandt and M. Indenbom, Phys. Rev. B **48**, 12 893 (1993); Physica B **194-196**, 1803 (1994); see also W. T. Norris, J. Phys. D **3**, 489 (1970).
[26] E. Zeldov, J. R. Clem, M. McElfresh, and M. Darwin, Phys. Rev. B **49**, 9802 (1994).
[27] J. R. Clem and A. Sanchez, Phys. Rev. B **50**, 9355 (1994).
[28] J. Gilchrist, Physica (Amsterdam) C **219**, 67 (1994).
[29] E. H. Brandt, Phys. Rev. Lett. **71**, 2821 (1993).
[30] E. H. Brandt, Phys. Rev. B **49**, 9024 (1994).
[31] E. H. Brandt, Phys. Rev. B **50**, 4034 (1994).
[32] J. Kötzler, G. Nakielski, M. Baumann, R. Behr, F. Goerke, and E. H. Brandt, Phys. Rev. B **50**, 3384 (1994).
[33] E. H. Brandt, Physica (Amsterdam) C **73**, 1731 (1994).
[34] A. Gurevich and E. H. Brandt, Phys. Rev. Lett. **73**, 178 (1994).
[35] J. Provost, E. Paumier, and A. Fortini, J. Phys. F **4**, 439 (1974).
[36] M. Indenbom and E. H. Brandt, Phys. Rev. Lett. **73**, 1731 (1994).
[37] T. B. Doyle (unpublished).
[38] E. Zeldov, A. I. Larkin, V. B. Geshkenbein, M. Konczykowski, D. Majer, B. Khaykovich, V. M. Vinokur, and H. Shtrikman, Phys. Rev. Lett. **73**, 1428 (1994).
[39] Th. Schuster, M. V. Indenbom, H. Kuhn, E. H. Brandt,

and M. Konczykowski, Phys. Rev. Lett. **73**, 1424 (1994).
[40] L. Burlachkov, Phys. Rev. B **47**, 8056 (1993).
[41] M. V. Indenbom, Th. Schuster, M. R. Koblischka, A. Forkl, H. Kronmüller, L. A. Dorosinskii, V. K. Vlasko-Vlasov, A. A. Polyanskii, R. L. Prozorov, and V. I. Nikitenko, Physica (Amsterdam) C **209**, 259 (1993).
[42] K.-H. Greubel, E. Gmelin, N. Moser, Ch. Mensing, and L. Walz, Cryogenics (Suppl.) **30**, 457 (1990).
[43] M. R. Koblischka, N. Moser, B. Gegenheimer, and H. Kronmüller, Physica (Amsterdam) C **166**, 36 (1990).
[44] A. Forkl, H.-U. Habermeier, B. Leibold, T. Dragon, and H. Kronmüller, Physica (Amsterdam) C **180**, 155 (1991).
[45] M. Qvarford, K. Heeck, J. G. Lensink, R. J. Wijngaarden, and R. Griessen, Rev. Sci. Instrum. **63**, 5726 (1992).
[46] J. C. Martinez, S. H. Brongersma, D. G. de Groot, R. Griessen, B. Ivlev, and P. H. Kes, Phys. Rev. Lett. **69**, 2276 (1992).
[47] H. G. Schnack, R. Griessen, J. G. Lensink, C. J. van der Beek, and P. H. Kes, Physica (Amsterdam) C **197**, 337 (1992).
[48] L. Pust, J. Kadlecova, M. Jirsa, and S. Durcok, J. Low Temp. Phys. **78**, 179 (1990); M. Jirsa, L. Pust, H. G. Schnack, and R. Griessen, Physica (Amsterdam) C **207**, 85 (1993).
[49] H. U. Habermeier, Eur. J. Solid State Inorg. Chem. **28**, 619 (1991).
[50] T. W. Li, P. H. Kes, N. T. Hien, J. J. M. Franse, and A. A. Menovsky, J. Crystal Growth **135**, 481 (1994).
[51] L. Civale, A. D. Marwick, T. K. Worthington, M. A. Kirk, J. A. Thompson, L. Krusin-Elbaum, Y. Sun, J. R. Clem, and F. Holtzberg, Phys. Rev. Lett. **67**, 648 (1991); M. Konczykowski, F. Rullier-Albenque, E. R. Yacobi, A. Shaulov, Y. Yeshurun, and P. Lejay, Phys. Rev. B **44**, 7167 (1991); W. Gerhäuser, G. Ries, H.-W. Neumüller, W. Schmitt, O. Eibl, G. Saemann-Ischenko, and S. Klaumünzer, Phys. Rev. Lett. **68**, 879 (1992); V. Hardy, J. Provost, D. Groult, M. Hervieu, B. Raveau, S. Durcok, E. Pollert, J. C. Frison, J. P. Chaminade, and M. Pouchard, Physica (Amsterdam) C **201**, 85 (1992); M. Leghissa, Th. Schuster, W. Gerhäuser, S. Klaumünzer, M. R. Koblischka, H. Kronmüller, H. Kuhn, H.-W. Neumüller, and G. Saemann-Ischenko, Europhys. Lett. **11**, 323 (1992); Th. Schuster, M. R. Koblischka, H. Kuhn, H. Kronmüller, M. Leghissa, W. Gerhäuser, G. Saemann-Ischenko, H.-W. Neumüller, and S. Klaumünzer, Phys. Rev. B **46**, 8496 (1992); Th. Schuster, M. Leghissa, M. R. Koblischka, H. Kuhn, H. Kronmüller, and G. Saemann-Ischenko, Physica (Amsterdam) C **203**, 203 (1992).
[52] G. D.'Anna, M.-O. André, M. V. Indenbom, and W. Benoit, Physica (Amsterdam) C **230**, 115 (1994).
[53] Th. Schuster, M. V. Indenbom, M. R. Koblischka, H. Kuhn, and H. Kronmüller, Phys. Rev. B **49**, 3443 (1994).
[54] Th. Schuster, M. R. Koblischka, N. Moser, and H. Kronmüller, Physica (Amsterdam) C **179**, 269 (1991).
[55] Th. Schuster, M. R. Koblischka, B. Ludescher, and H. Kronmüller, J. Appl. Phys. **72**, 1478 (1992).
[56] Th. Schuster, M. R. Koblischka, H. Kuhn, B. Ludescher, M. Lippert, and H. Kronmüller, Physica (Amsterdam) C **196**, 373 (1992).
[57] V. K. Vlasko-Vlasov, M. V. Indenbom, V. I. Nikitenko, A. A. Polyanskii, R. L. Prozorov, I. V. Grekhov, L. A. Delimova, I. A. Liniichuk, A. V. Antonov, and M. Yu. Gusev, Superconductivity **5**, 1582 (1992).
[58] A. M. Campbell and J. E. Evetts, *Critical Currents in Superconductors* (Taylor & Francis, London, 1972), p. 71.
[59] R. P. Huebener, R. T. Kampwirth, and J. R. Clem, J. Low Temp. Phys. **6**, 275 (1972).
[60] M. V. Indenbom, H. Kronmüller, T. W. Li, P. H. Kes, and A. A. Menovsky, Physica (Amsterdam) C **222**, 203 (1994).

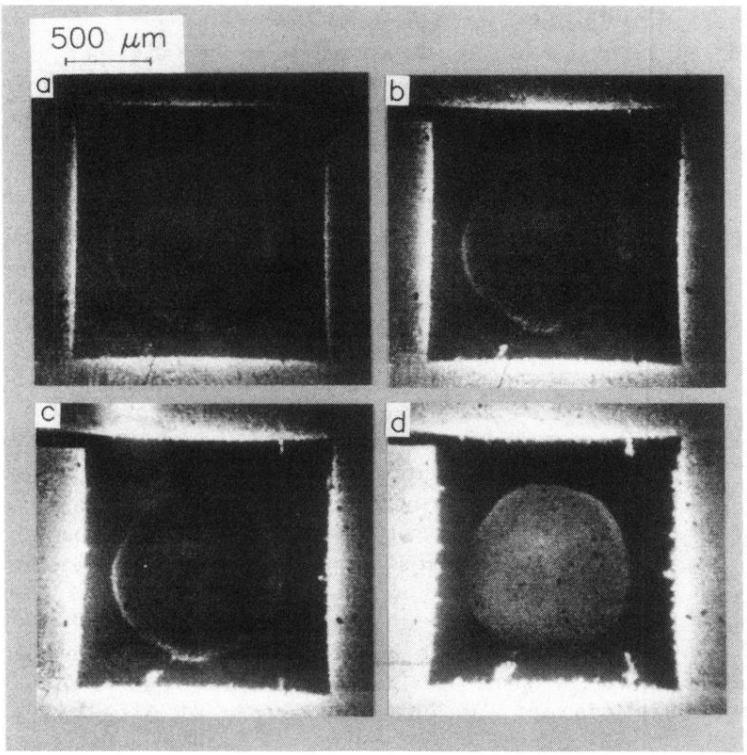

FIG. 12. Flux distribution of a ring-shaped YBCO thin film obtained at $T = 5$ K. (a) $\mu_0 H_a = 11$ mT, (b) $\mu_0 H_a = 16$ mT, (c) $\mu_0 H_a = 21$ mT, (d) $\mu_0 H_a = 42$ mT. Here, magnetic flux has penetrated into the inner hole at the defect structure which is visible near the lower left sample corner. The small bridge at the left sample edge is part of the voltage tap. For details see text.

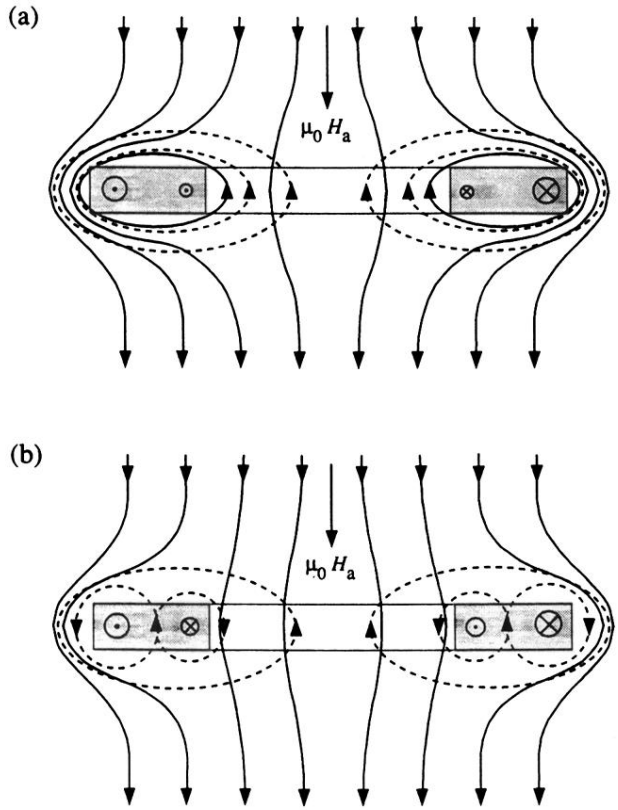

FIG. 13. Sketch of the magnetic field lines and the direction of current flow. The current-generated magnetic field is plotted as dashed lines, whereas the superposition of the homogeneous external magnetic field $\mu_0 H_a$ and current-generated field is drawn as solid lines. $\odot$ symbolizes the current which flows out of the drawing plane; $\otimes$ is the opposite flowing direction. (a) No flux has penetrated from outside the ring into the central hole. The equal numbers of field lines of opposite direction symbolizes $\Phi = 0$ in the central hole. (b) At one particular place the flux front has reached the inner edge of the ring and magnetic flux leaks into the central hole where now $\Phi > 0$.

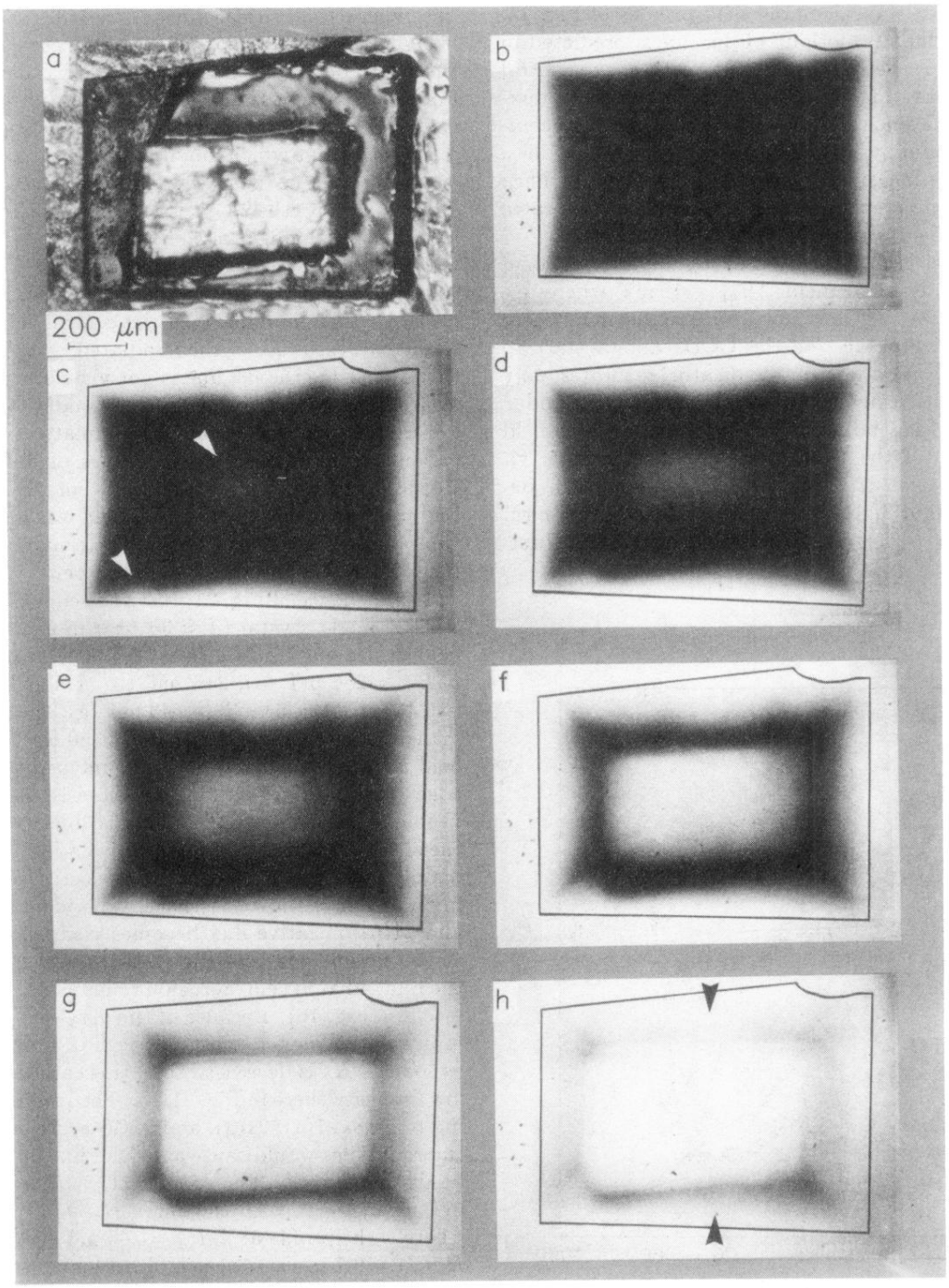

FIG. 19. (a) Shape of the irradiated Bi2212 single crystal. The absorber is visible as bright region in the sample center. (b) Flux distribution at $T = 50$ K in a transverse magnetic field of $\mu_0 H_a = 85$ mT. (c) $\mu_0 H_a = 107$ mT. The flux starts to penetrate the unirradiated part of the sample at the narrowest place of the irradiated belt (white arrow in the lower left corner) and piles up in the sample center as indicated by the other white arrow. (d) $\mu_0 H_a = 128$ mT. (e) $\mu_0 H_a = 149$ mT. (f) $\mu_0 H_a = 171$ mT. (g) $\mu_0 H_a = 213$ mT. (h) $\mu_0 H_a = 277$ mT.

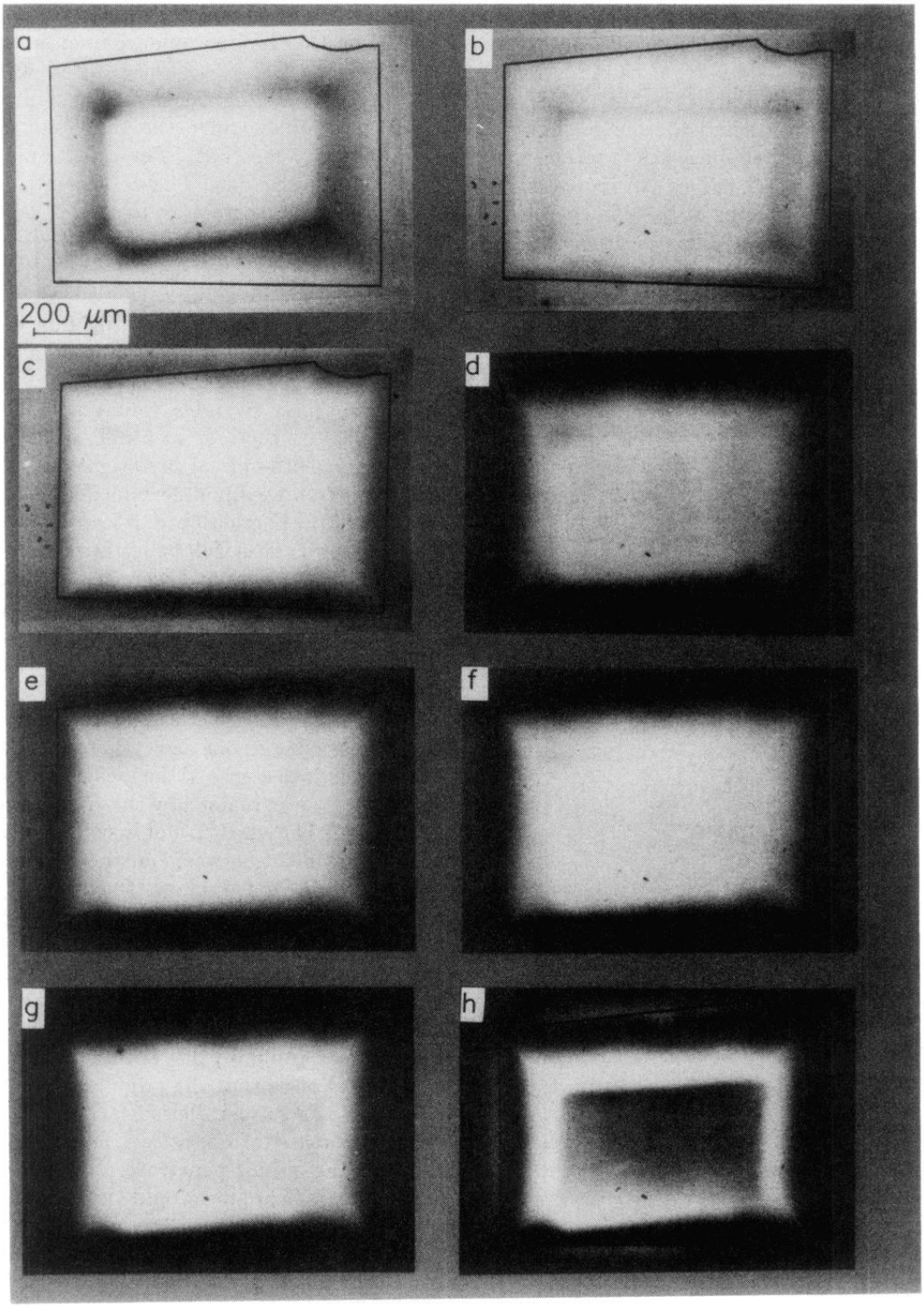

FIG. 21. Flux distributions of the same Bi2212 single crystal at $T = 50$ K. In these experiments the external magnetic field is decreased from $\mu_0 H_0 = 277$ mT to various external fields $\mu_0 H_a$. (a) $\mu_0 H_a = 256$ mT, (b) $\mu_0 H_a = 213$ mT, (c) $\mu_0 H_a = 177$ mT, (d) $\mu_0 H_a = 128$ mT, (e) $\mu_0 H_a = 107$ mT, (f) $\mu_0 H_a = 64$ mT, (g) $\mu_0 H_a = 43$ mT, (h) $\mu_0 H_a = 0$ mT (remanent state).

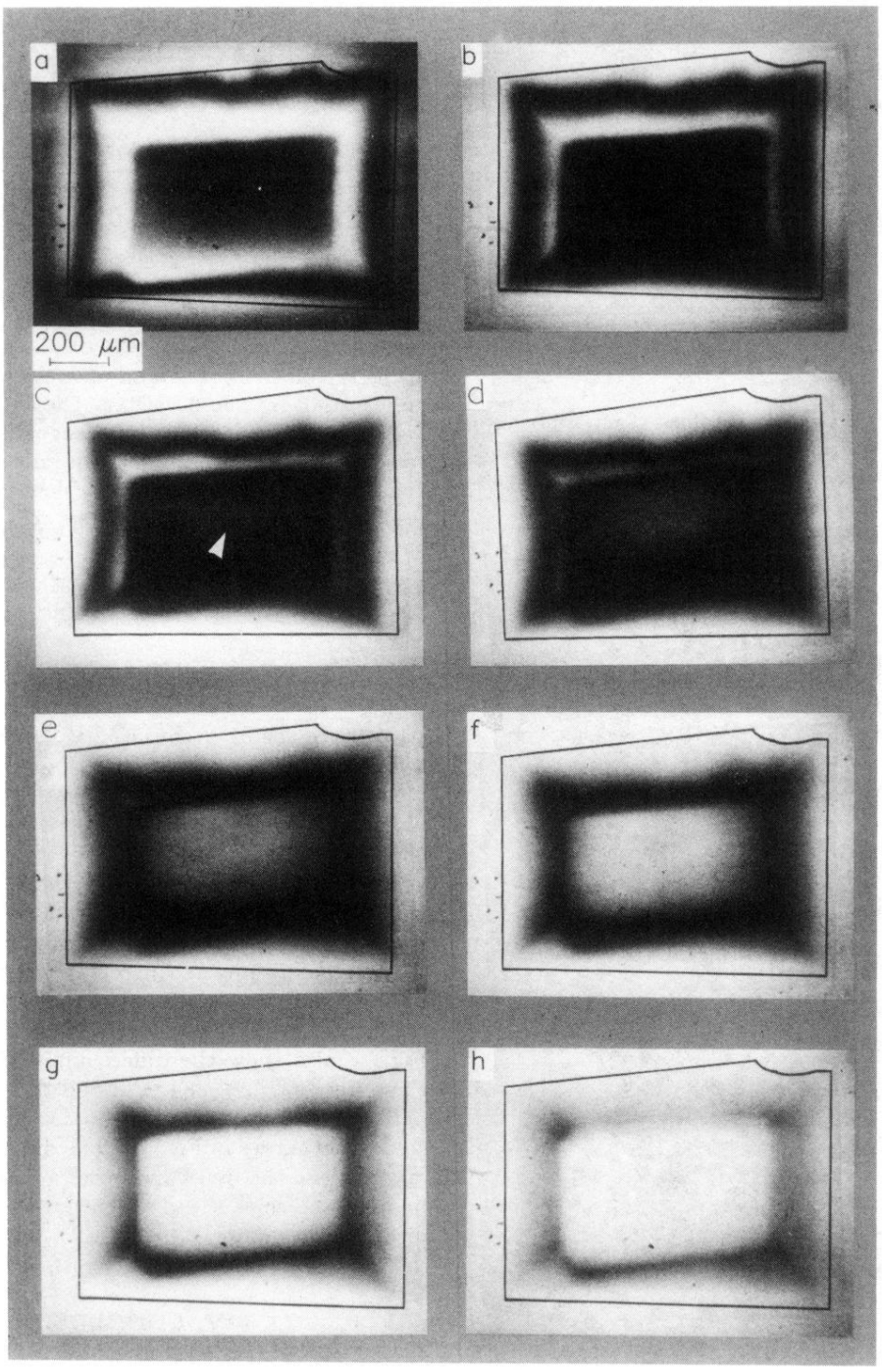

FIG. 23. Flux distribution of the edge-zone-irradiated Bi2212 single crystal when applying a reversed field H_a to the remanent state. (a) $\mu_0 H_a = -21$ mT, (b) $\mu_0 H_a = -85$ mT, (c) $\mu_0 H_a = -100$ mT; here negative flux has started to penetrate the unirradiated zone (white arrow). (d) $\mu_0 H_a = -128$ mT, (e) $\mu_0 H_a = -149$ mT, (f) $\mu_0 H_a = -171$ mT, (g) $\mu_0 H_a = -213$ mT, (h) $\mu_0 H_a = -277$ mT.

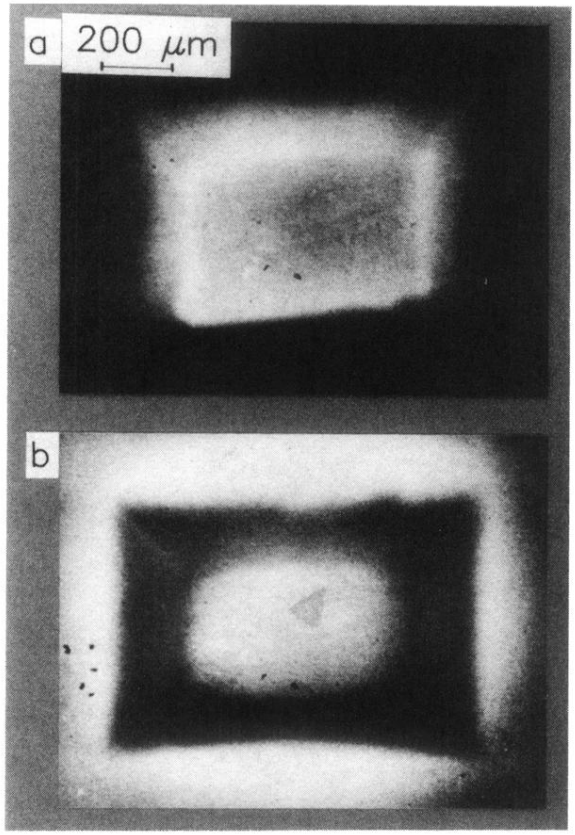

FIG. 25. Field-cooling experiments performed on the edge-zone-irradiated Bi2212 single crystal. The sample was cooled down to $T = 50$ K in an applied field of $\mu_0 H_a = 64$ mT. (a) $\mu_0 H_a = 21$ mT, (b) $\mu_0 H_a = 107$ mT. For details see text.

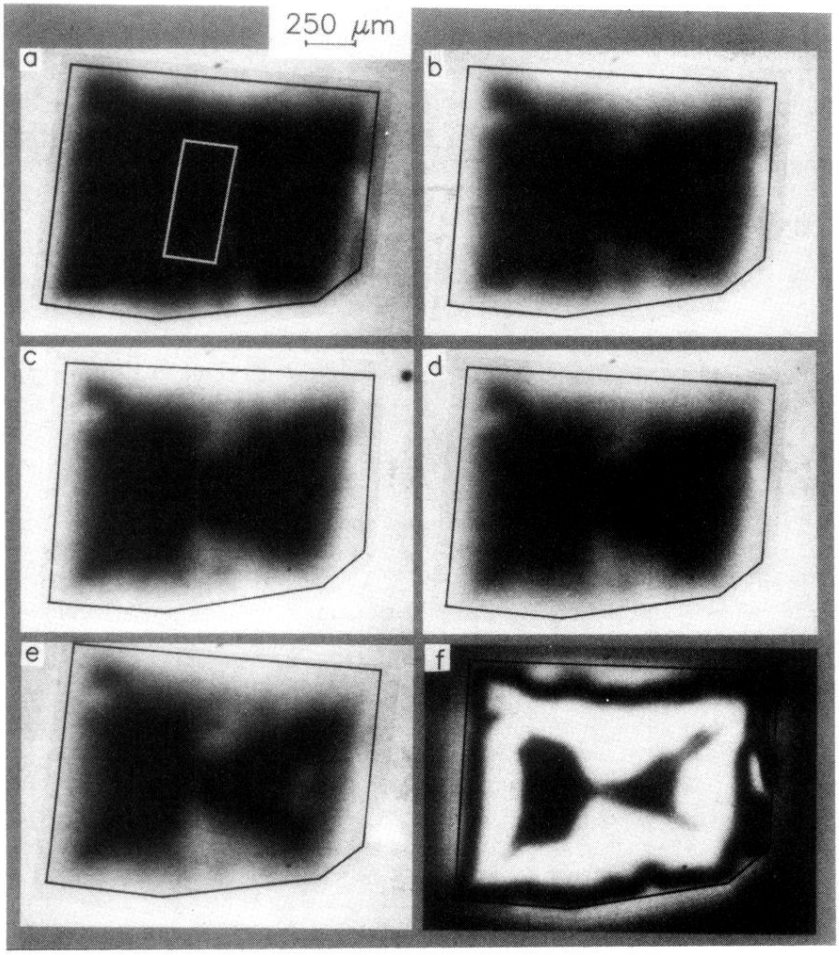

FIG. 27. Flux distributions in a Bi2212 single crystal with thinned central region at T = 20 K. (a) $\mu_0 H_a$ = 384 mT; the white frame indicates the thinned-down region. (b) $\mu_0 H_a$ = 427 mT, (c) $\mu_0 H_a$ = 469 mT, (d) $\mu_0 H_a$ = 513 mT, (e) $\mu_0 H_a$ = 534 mT, (f) remanent state of (e).

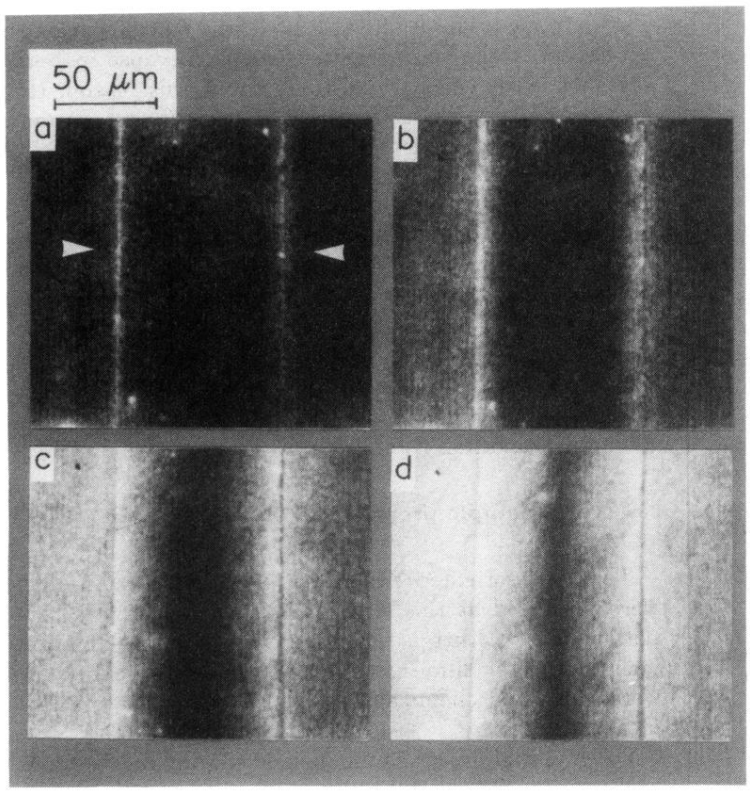

FIG. 3. Flux distributions of 82 μm wide and 300 nm thick YBCO strip obtained by means of EuSe as magneto-optical indicator. The external magnetic field $\mu_0 H_a$ is oriented perpendicular to the sample surface and hence parallel to the c axis. The bright areas of the sample show the Shubnikov phase; the dark regions correspond to the flux-free Meissner phase. (a) $\mu_0 H_a$ = 21 mT. The white arrows indicate the place where the profiles in Fig. 4 were measured. (b) $\mu_0 H_a$ = 53 mT, (c) $\mu_0 H_a$ = 107 mT, (d) $\mu_0 H_a$ = 160 mT.

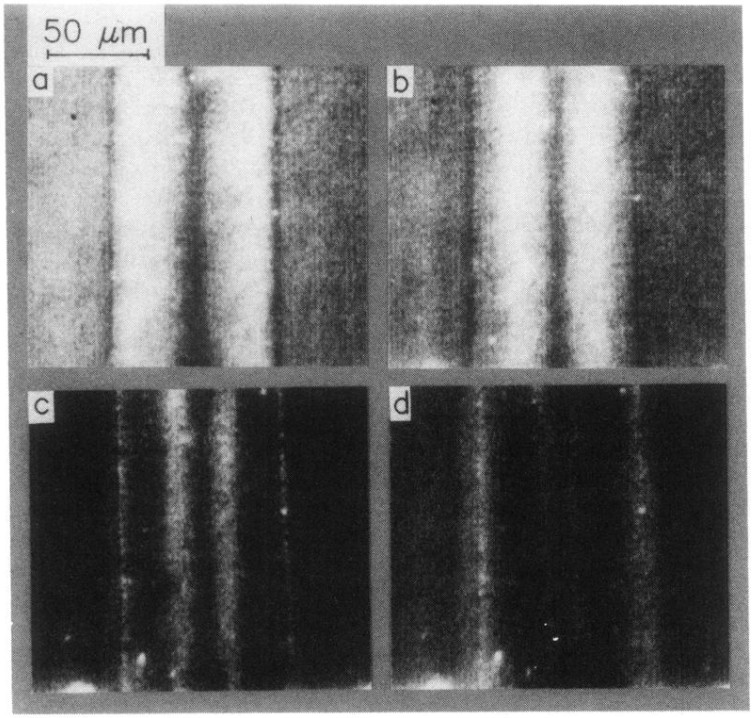

FIG. 5. Flux distributions on the same YBCO strip. In these experiments the external magnetic field is decreased from $\mu_0 H_a$ = 160 mT to various external fields $\mu_0 H_a$. (a) $\mu_0 H_a$ = 107 mT, (b) $\mu_0 H_a$ = 53 mT, (c) $\mu_0 H_a$ = 0 mT (remanent state), (d) $\mu_0 H_a$ = − 53 mT.

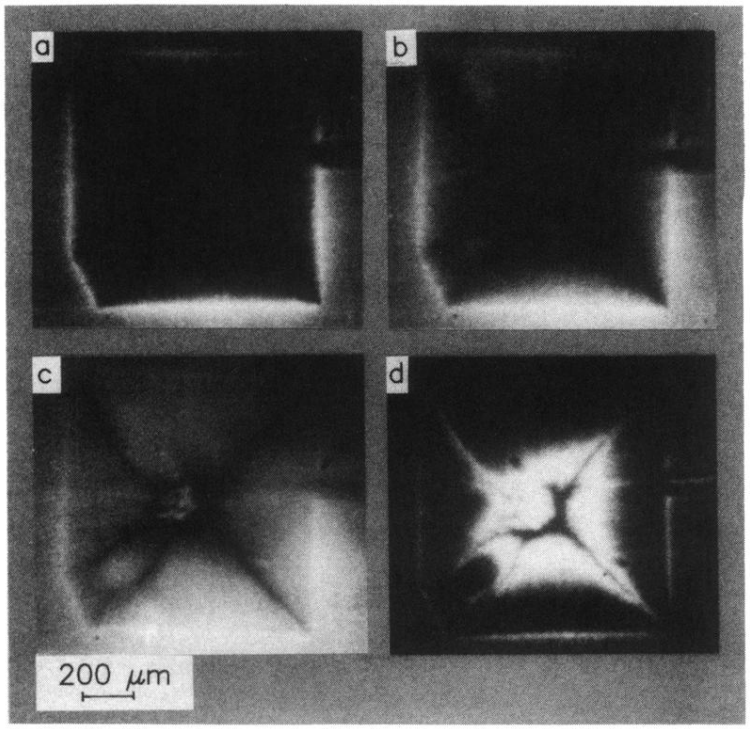

FIG. 8. Flux distributions of a nearly square patterned YBCO thin film (width 1 mm, thickness 300 nm). In this case an iron-garnet film was used as magneto-optical indicator. The external magnetic field $\mu_0 H_a$ is oriented perpendicular to the sample surface. (a) $\mu_0 H_a = 53$ mT, (b) $\mu_0 H_a = 107$ mT, (c) $\mu_0 H_a = 213$ mT, (d) $\mu_0 H_a = 0$ mT [remanent state of (c)].